

Atomic Layer Deposition Synthesis and Photoelectrochemical Charge Behavior in Tungsten, Iron, and Titanium Oxide Heterostructures

Author: Stafford Wheeler Sheehan

Persistent link: <http://hdl.handle.net/2345/2203>

This work is posted on [eScholarship@BC](#),
Boston College University Libraries.

Boston College Electronic Thesis or Dissertation, 2011

Copyright is held by the author, with all rights reserved, unless otherwise noted.

Atomic Layer Deposition Synthesis and Photoelectrochemical Charge Behavior in Tungsten, Iron, and Titanium Oxide Heterostructures

Stafford Wheeler Sheehan

Undergraduate Thesis

Advisor: Prof. Dunwei Wang

Table of Contents:

1. Chapter 1: Introduction

- a. 1.1 Solar Cells
 - i. 1.1.1 Brief History
 - ii. 1.1.2 General Working Principle of Solar Cells
 - iii. 1.1.3 Photoelectrochemical (PEC) Cells
 - iv. 1.1.4 Theoretical Efficiency and Thermodynamic Considerations
- b. 1.2 Charge Transfer in Semiconductors
 - i. 1.2.1 Charge Transfer and Decay
- c. 1.3 Photoanodes for Water Oxidation
 - i. 1.3.1 Processes at the Electrode Surface
- d. 1.4 Goals of this Study

2. Chapter 2: Materials and Methods

- a. 2.1 Synthesis and Characterization Techniques
 - i. 2.1.1 Atomic Layer Deposition (ALD)
 - ii. 2.1.2 Solid State Characterization
 - iii. 2.1.3 PEC Characterization
 - iv. 2.1.4 Time-Resolved Microwave Conductivity (TRMC)
- b. 2.2 Materials
 - i. 2.2.1 Tungsten Trioxide
 - ii. 2.2.2 Iron Oxide
 - iii. 2.2.3 Titanium Dioxide

3. Chapter 3: ALD Synthesis and Characterization of WO_3 , Fe_2O_3 , and $\text{Ti}_{0.7}\text{W}_{0.3}\text{O}_2$ Thin Films

- a. 3.1 Synthesis of WO_3 Thin Film
 - i. 3.1.1 Low and High Growth Rate Syntheses
 - ii. 3.1.2 Post-Growth Treatment
- b. 3.2 Application of WO_3 Synthesis to $\text{Ti}_{0.7}\text{W}_{0.3}\text{O}_2$ Thin Films
 - i. 3.2.1 Growth and Characterization of $\text{Ti}_{0.7}\text{W}_{0.3}\text{O}_2$ Thin Films
- c. 3.3 Synthesis of Fe_2O_3 Thin Film
 - i. 3.3.1 Synthesis of $[\text{Fe}(\text{O}^t\text{Bu})_3]_2$ Precursor and Fe_2O_3 Thin Film Growth

4. Chapter 4: Photocatalysis with Heterostructured Photoanodes

- a. 4.1 TiSi_2 Nanonet Heterostructures for Water Splitting

- i. 4.1.1 TiO₂/TiSi₂
 - ii. 4.1.2 Ti_{0.7}W_{0.3}O₂/TiSi₂
 - iii. 4.1.3 WO₃/TiSi₂
 - iv. 4.1.4 Fe₂O₃/TiSi₂
- b. 4.2 4-Chlorophenol Photocatalysis with Silica/WO₃ Heterostructures

5. Chapter 5: Investigation of Charge Carrier Dynamics with Time-Resolved Microwave Photoconductivity (TRMC)

- a. 5.1 Charge Transfer at the Interface
- b. 5.2 Long Carrier Lifetime in Heteronanostructures
- c. 5.3 Changes in Observed Lifetime with pH
 - i. 5.3.1 Iron Oxide
 - ii. 5.3.2 Tungsten Oxide

6. Conclusions and Further Work

7. Publications

8. Acknowledgements

Chapter 1

Introduction

1.1 Solar Cells

One of the most critical issues facing today's society is the development of a sustainable and cost effective method of harvesting energy. As technology becomes more readily available to developing countries, the global demand of energy will continue to increase while supply remains relatively constant. This may have severe ramifications on human health, global economy, and every aspect of modern life if new methods of harvesting energy are not identified.

Currently, the majority of energy generated for human consumption comes from fossil fuels. In addition to being a non-renewable resource with byproducts that may have a negative effect on the environment, there is economic stimulus to discover alternative sources of energy due to increasing fuel prices. Of these new approaches to energy harvesting, solar energy is both the safest and has the highest potential, with more energy in the form of sunlight striking Earth in one hour (4.3×10^{20} J) than is consumed in a full year (4.1×10^{20} J).¹

There are significant technological hurdles, however, that must be overcome in order for solar energy to be cost-competitive with fossil fuels. The major limitation of using solar cells as a viable energy source is its initial cost when compared to other forms of fuel.

¹ Lewis, N. S. *Science* **2007**, 315, 798

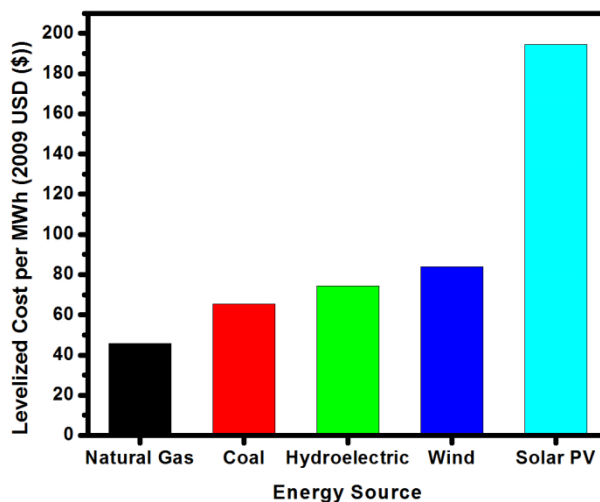


Figure 1.1 Cost comparison of different energy sources for power plants that had begun construction in 2010 and scheduled to be completed on or before 2016.²

Parallel to this is a cost-efficiency dilemma; the more efficient a solar cell is, the more expensive it is going to be to produce due to scarcity of rare-earth elements and/or costly synthesis requirements. For example, in order to produce monocrystalline silicon (mono-Si) used in many high efficiency photovoltaic cells, silicon must be annealed at much higher temperatures than is necessary to produce a lower efficiency amorphous silicon photovoltaic cell.³ The cost of this additional heat energy compounded with other synthesis requirements can greatly increase the overall cost of a mono-Si photovoltaic array to the point where it would be cost-prohibitive for many individuals to own them. Because of this, new synthesis methods are being developed and other materials are being explored to more efficiently harvest and store solar energy at a cheaper system cost.

This chapter focuses on the fundamental science behind solar cells. Briefly, a history of solar cells from the discovery of the photovoltaic effect to recent years will be covered, followed by the basic design principles of photovoltaic cells. Photoelectrochemical (PEC) cells will then be outlined briefly, followed by a more focused discussion of photoanodes in section 1.3. The end of section 1.1 and section 1.2 will deal with the physical chemistry and solid state physics of solar cells, including thermodynamic efficiency limits and charge generation and transport. The chapter will conclude with the goals of this project, segueing into the research reported in this thesis on nanostructured photoanodes.

² Levelized cost per MWh is the amount that the power plant would have to charge consumers per MWh every year throughout its operation in order to make up for production, maintenance, overhead, and fuel costs. Data from: Energy Information Administration (2010) *Annual Energy Outlook 2011* (US Dept of Energy, Washington, DC).

³ Solar Energy Utilization Workshop (2005) *Basic Science Needs for Solar Energy Utilization* (US Dept of Energy, Washington, DC).

1.1.1 Brief History

Solar cells operate by exploiting the photovoltaic effect, discovered by Edmund Becquerel in 1839 when he showed a voltage and current produced from an AgCl electrode in an electrolyte when connected to a metal counter electrode and irradiated with white light.⁴ A similar effect was seen in 1877 by W. Adams and R. Day with a solid state selenium system.⁵ 77 years later, in 1954, D. Chapin, C. Fuller, and G. Pearson at Bell Labs developed a p-n junction based photovoltaic cell using monocrystalline silicon with a sunlight-to-electricity energy conversion efficiency of over 5%.⁶ Development of the silicon p-n junction solar cell was a critical turning point in realizing solar cells as an energy source and was the forerunner to modern day photovoltaic cells.

For the next 20 years, solar cell development was explored primarily to power space shuttles and satellites. A cadmium sulfide solar cell was developed by D. Reynolds, G. Leies, L. Antes, and R. Margburger later in 1954, and the race to develop higher efficiency solar cells began.⁷ Research was focused primarily on generation of energy from sunlight and not on storage until the early 1970s when an oil crisis spurred the world to search for alternative energy sources. This made the discovery of TiO₂ based water splitting photoelectrochemical cells by A. Fujishima and K. Honda in 1972 another turning point in solar cell research.⁸ This system not only converted high energy photons into fuel, it stored that energy in the chemical bonds of hydrogen and oxygen gas so that it could be used at a later point and required only water and sunlight to operate.

Parallel to this, the field of nanotechnology was in its infant stages. In 1959, Richard Feynman's lecture, *There's Plenty of Room at the Bottom*, spurred on research at the nanoscale.⁹ This led to many attempts to exploit properties of materials at the nanoscale in order to produce more efficient solar cells. In 1964, R. Wagner and W. Ellis at Bell Labs reported the vapor-liquid-solid (VLS) synthesis of silicon nanowires using gold droplets as catalysts, leading to many attempts at using silicon nanowires in a photovoltaic cell.¹⁰ Porous structures and monolayers closely followed.¹¹

Research in integration of nanomaterials to photovoltaic and photoelectrochemical systems continues, though no commercially available system exists yet. Nanomaterials are interesting for energetic applications for a variety of reasons, including but not limited to: high surface area resulting in many catalytically active surface sites, size tunability of the same scale as the wavelengths of visible light, and improved charge transport by possessing sizes close to the diffusion length of charges. When tuned appropriately, these attributes can be very advantageous in solar cell design.

⁴ Becquerel, E. *Comptes Rendus* **1839**, 9, 561.

⁵ Adams, W. G.; Day, R. E. *Proc. R. Soc. London Ser. A* **1877**, 25, 113.

⁶ Chapin, D. M.; Fuller, C. S.; Pearson, G. L. *J. Appl. Phys.* **1954**, 25, 676.

⁷ Reynolds, D. C.; Leies, G.; Antes, L. L.; Marburger, R. E. *Phys. Rev.* **1954**, 96, 533.

⁸ Honda, K.; Fujishima, A. *Nature* **1972**, 238, 37.

⁹ Feynman, R. P. *Caltech Engineering and Science* **1960**, 23, 22.

¹⁰ Wagner, R. S.; Ellis, W. C. *Appl. Phys. Lett.* **1964**, 4, 89.

¹¹ Kim, Y. S.; Liang, K. N.; Law, K. Y.; Whitten, D. G. *J. Phys. Chem.* **1994**, 98, 984.

1.1.2 General Working Principles of Solar Cells

A solar cell is, by definition, a device that uses the photovoltaic effect to convert solar light to electricity. In order to do this, there must be a material that absorbs light and uses that energy to separate electrons and electron holes, creating an electric field through photoinduced charge separation. In addition to this, there must be two electrodes to collect these charges, one to collect electrons and one to collect holes. Generally, the photoactive material is sandwiched between the two electrodes.

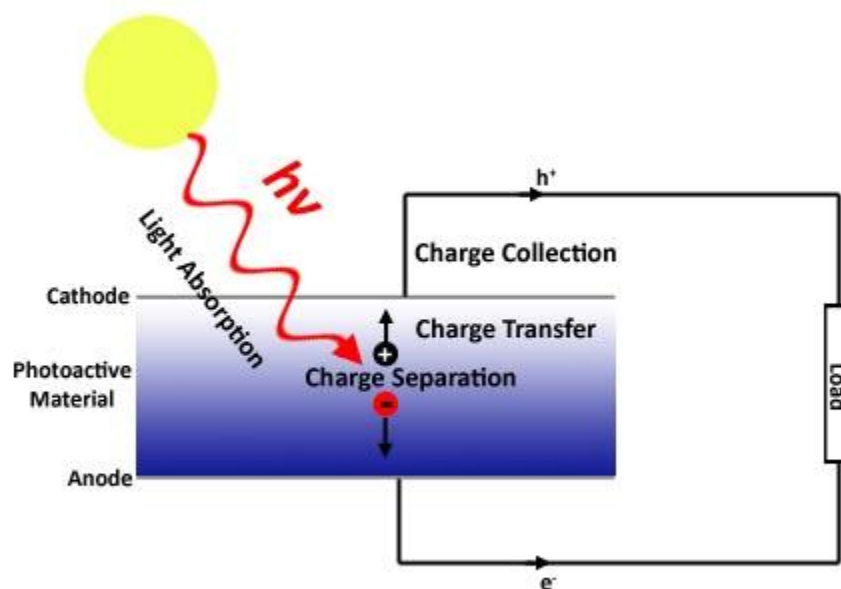


Figure 1.2 Schematic representation of a solar cell. Illumination through a transparent electrode results in the generation of excitons (bound electron-hole pairs) in the active material. These excitons are separated into free electrons and holes and collected at the electrodes.

There are four essential steps that all solar cells have in common (Figure 1.2): light absorption, charge separation, charge transport, and charge collection. Each can be optimized individually, but in many cases optimizing one step significantly hinders one or more of the others. For example, a thick solar cell will be able to absorb more than a thin solar cell, but requires charges to travel farther in order to be collected which increases the chance that they encounter charge traps and recombination centers.

When light is absorbed by a solar cell electrons are excited from a photoactive material's valence band to its conduction band leaving behind positive electron holes. While the electron and hole are still attracted to each other by Coulomb forces they behave as a single object and thus exist in a bound state until they are spatially separated by an electric field. Inorganic semiconductors are unique in that they have high dielectric constants which promote charge separation out of this excitonic bound state. In p-n junction photovoltaic cells the electric field is caused by charge migration at the interface of the n-type and p-type semiconductor.

When a p-type semiconductor and an n-type semiconductor are brought into contact, electron flow occurs between them to equilibrate their electrochemical potentials (Fermi levels). This forms an electric field, which results in charge accumulation near the interface (for example, in the n-type semiconductor a positive charge will be present in the dopant ions near

the junction). As a result of this, the energy bands of each semiconductor will bend at the p-n junction making it energetically favorable for holes to travel to the cathode and electrons to travel to the anode (Figure 1.3).

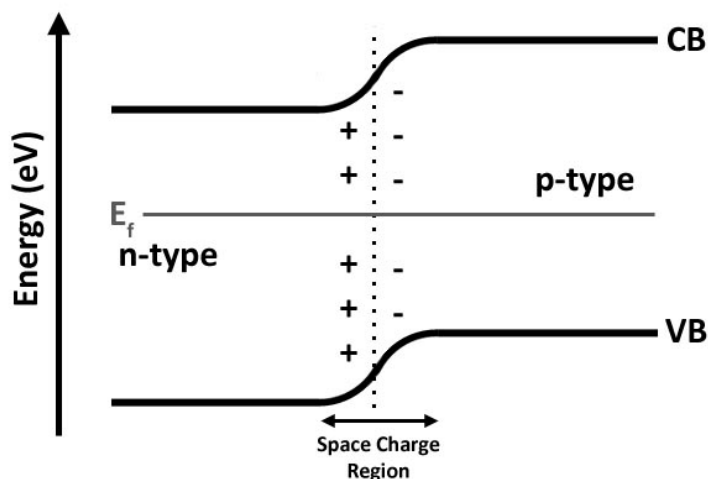


Figure 1.3 Band energy diagram for a p-n junction at equilibrium; without illumination and with no external bias. Note that the electric field pushes charges in the opposite direction of charge diffusion. This is due to the system being in thermal equilibrium.

This equilibrium is broken when the p-n junction system is placed under illumination. When photons with energy greater than or equal to the band gap of the semiconductor are absorbed, the material undergoes a change in its dielectric constant. This causes a change in the relative carrier density of majority and minority carriers, which separates the electrochemical potentials of electrons and holes in the semiconductor. A result of this is the formation of a hole quasi-Fermi level ($E_{f,n}$) and an electron quasi-Fermi level ($E_{f,p}$) (Figure 1.4). Since the electric field strength in the semiconductor depends on the energy difference between the semiconductors' Fermi levels, the maximum voltage generated by the junction under illumination (open circuit potential, V_{oc}) is given by the energy difference between $E_{f,n}$ and $E_{f,p}$. A high V_{oc} promotes separation of electrons and holes; this helps to drive excited electrons to the n-type region while holes travel toward the p-type region.

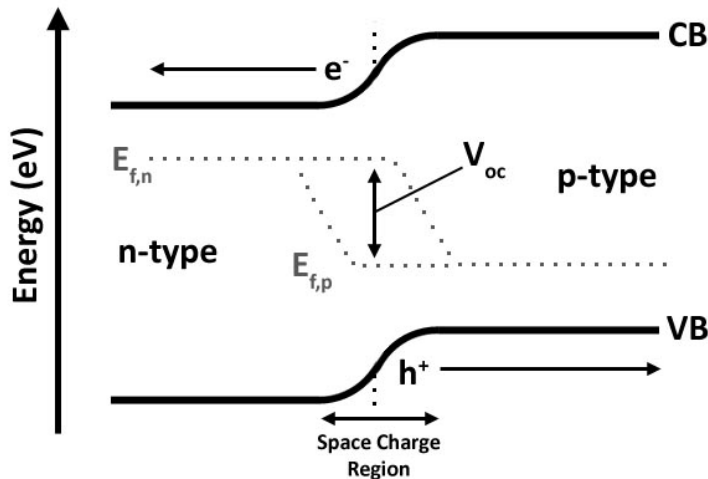


Figure 1.4 Band energy diagram for a p-n junction under illumination with photon energy at or greater than the material's band gap, E_g .

While V_{oc} governs charge separation and is dependent on junction quality, band gap, defect density, and dopant concentration, short circuit current (I_{sc}) depends on illumination intensity, absorbance, and recombination losses prior to charge collection. I_{sc} is representative of the maximum number of photogenerated charge carriers per unit area that are extracted from the solar cell. Generally, I_{sc} decreases with increasing band gap since less light is absorbed overall and V_{oc} increases as band gap increases. This, and definitions of V_{oc} and I_{sc} in a semiconductor will be further explored in section 1.2.1.

After light absorption and exciton generation, charges must be separated and rapidly transported away from the junction before recombination can occur. This can be done by ensuring the photoactive materials are thinner than its minority carrier diffusion length, synthesizing highly crystalline materials with low defect density to prevent charge trapping/recombination, and improving the interface between the electrode and photoactive material.

1.1.3 Photoelectrochemical Cells

Photoelectrochemical (PEC) cells operate with the same basic principles as solar cells; a photoactive material absorbs sunlight to excite electrons to the conduction band and form electron-hole pairs. The major difference between PEC cells and solid state photovoltaic cells is the presence of a liquid electrolyte between anode and cathode that is used as a medium to transport and/or store charge. Currently there are two different types of PEC cells that are being researched intensely: regenerative cells and photosynthetic cells (Figure 1.5).¹²

Regenerative cells convert photons to electric charge without any chemical change. In a similar fashion to photovoltaic cells, photons incident on the cell with $E > E_g$ generate electron-hole pairs that become separated by the electric field present in the semiconductor's space charge

¹² Gratzel, M. *Nature* 2001, 414, 338.

region. Majority carriers move through the semiconductor to the external circuit, similarly to p-n junction photovoltaic cells. Minority carriers, however, are driven to the semiconductor-liquid junction where they oxidize a hole scavenger (the reduced form of the redox couple present). As electrons enter the solution from the cathode, the oxidized form of the redox couple is reduced again forming a complete circuit. Dye-sensitized solar cells (DSSCs) are an example of a regenerative cell that uses dyed TiO_2 as a photoactive anode, platinum as a cathode, and an I_2/I^- redox couple.¹³ It is also notable that this is the only type of DSSC with high enough efficiency and low enough cost to be in commercial production.

The second type of PEC cell is a photosynthetic cell. Instead of forming a closed circuit like most other solar cells, photosynthetic cells use sunlight to generate electron-hole pairs that are used to split water into H_2 and O_2 to be used as fuel. This system is more complex than regenerative systems since there are two different redox reactions happening: the four electron process of oxidizing water into O_2 , and the two electron process of reducing water to H_2 . As mentioned previously, this was first developed by K. Honda and A. Fujishima with TiO_2 .⁸ The drawback to this approach is the large band gap of TiO_2 ; it only absorbs UV light which is a tiny portion of the solar spectrum.

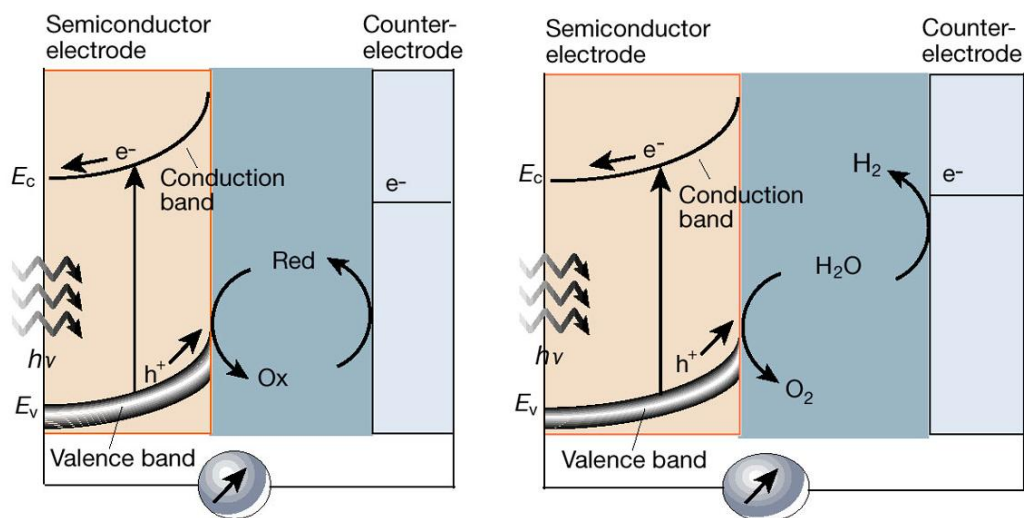


Figure 1.5 Band energy diagram for regenerative (left) and photosynthetic (right) PEC cells. Reproduced from [12].

While band bending and majority carrier transport properties in photoanodes/cathodes of PEC cells are similar to that of solid state p-n junction devices, transfer of minority carriers into solution may involve multiple steps and can be much more complex. This complexity, specifically in photosynthetic cells, had made progress in this field particularly difficult. The electrochemistry and thermodynamics of photosynthetic cells is covered further in section 1.3.

¹³ O'Regan, B.; Grätzel, M. *Nature* **1991**, 353, 737.

1.1.4 Theoretical Efficiency and Thermodynamic Considerations

Solar cells are subject to the same restrictions as any other thermodynamic system, this places limits on the maximum energy conversion efficiencies for different types of solar cells. The second law of thermodynamics states that the system will never have perfect efficiency since it is an energy transfer process; entropy will always cause some losses. Another way to think of this is by comparing a solar cell to a Carnot engine, there is a hot source (the sun), a cold sink (the solar cell), and work done in the form of charge transfer. The only way to achieve an efficiency of unity in a Carnot engine is if the cold sink is lowered to zero degrees Kelvin, which is thermodynamically prohibited. Therefore, even if every component of a solar cell were fully optimized there would still be losses due to entropy. Specifically there are four mechanisms in which energy, and therefore efficiency, is lost: hot electron relaxation ($E_{\text{photon}} > E_g$), electron relaxation in the band gap ($E_{\text{photon}} < E_g$), thermodynamic losses, and electronic losses.

The largest efficiency losses in a single band gap system come from electronic relaxation when the system is irradiated with photons possessing energy higher or lower than its band gap.¹⁴ Higher energy photons are excited to sub-bands in the conduction band but rapidly cool to the conduction band edge within picoseconds or, in many cases, even faster.¹⁵ This releases excess energy in the form of heat instead of harnessing that energy for charge transfer. Photons with energy lower than the material's band gap are completely converted to heat since they do not possess enough energy to excite an electron to a stable energy level. With these losses in mind, in addition to thermodynamic and electronic losses inherent to all solar cells, the maximum efficiency attainable for a single band gap system is around 31% and is called the Shockley-Queisser limit.¹⁴ By comparison in the case of a hypothetical infinite band gap system that could negate these losses, its maximum efficiency would be 68% under unconcentrated sunlight.¹⁶

In an ideal system, the next biggest loss in efficiency comes from thermodynamic losses. Electronic excitation is by nature an internal energy. By the definition of Gibbs free energy:

$$\Delta G = \Delta U + W - T\Delta S \quad . \quad (1.1)$$

The effect of the second law of thermodynamics can be seen; entropic losses will always occur in an increasing manner as temperature increases. This can be impacted by previous loss mechanisms too, since non-radiative recombination will increase the temperature of the system. The entropy increase can also be seen conceptually, as electrons are excited to the conduction band they gain translational degrees of freedom which in turn increases entropy, and likewise electrons left in the valence band gain degrees of freedom as the number of holes increases (Figure 1.6).

¹⁴ Shockley, W.; Queisser, H. J. *J. Appl. Phys.* **1961**, 32, 510.

¹⁵ Sambur, J. B.; Novet, T.; Parkinson, B. A. *Science* **2010**, 330, 63.

¹⁶ De Vos, A. J. *J. Appl. Phys.* **1980**, 13, 839.

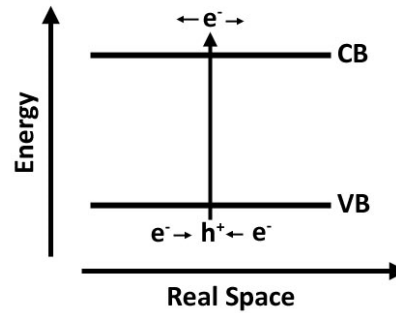


Figure 1.6 Band diagram illustrating increasing translational degrees of freedom for electrons in electronic excitation. This introduces additional entropy of mixing (ΔS_{mix}) to the system.

While thermodynamic losses can never be completely eliminated in an energy conversion system, they can be minimized. Returning to the comparison of a solar cell to a Carnot engine, one way to improve efficiency is by increasing the temperature of the heat source, T_{hot} , while leaving the temperature of the cold sink, T_{cold} , relatively constant. Though the temperature of the sun is constant, we can use solar concentrators to increase the effective T_{hot} that reaches the solar cell. Returning to the case of an infinite band gap system this would increase its theoretical maximum efficiency from 68% to 93% if it were placed under 46,200 suns.¹⁷

Finally, solar cells incur electronic losses. At the solar cell's maximum voltage, V_{oc} , the concentration of electrons in the conduction band is at its highest but any movement of charge will cause that concentration to decrease, thus current is zero. Meanwhile, at the solar cell's maximum current, I_{sc} , electrons are constantly flowing in and out of the system with no net concentration in the conduction band, therefore voltage is zero. In both cases, no work is done. Fill factor (FF) in a solar cell is a ratio of maximum obtainable power (voltage and current at its maximum power point on an I-V curve) to this maximum theoretical power ($V_{oc} \cdot I_{sc}$) and is representative of this electronic loss. FF can be optimized, thus minimizing electronic losses, by improving junction quality and reducing recombination in the cell. The characteristics V_{oc} and I_{sc} can be further derived mathematically from semiconductor physics, which we will now explore further.

1.2 Charge Transfer in Semiconductors

As stated previously, when light is irradiated on a system exhibiting the photovoltaic effect the photoactive material's dielectric constant changes, causing a change in carrier density. This is illustrated in the following continuity equation, in which diffusion processes are neglected for simplicity:

$$\frac{d\Delta p}{dt} = G - \frac{\Delta p}{\tau_p}, \quad (1.2)$$

¹⁷ Green, M. A. *Third Generation Photovoltaics: Advanced Solar Energy Conversion*, Springer-Verlag: Berlin, Germany, 2004.

where G is the charge generation rate and $\frac{\Delta p}{\tau_p}$ is the recombination rate in the semiconductor. The same relation also applies for negative electrons. As we inject carriers into the semiconductor at the surface with photons, there will be a homogeneous diffusion of excess carriers throughout the crystal lattice. The current given by this charge diffusion is proportional to the concentration gradient of carriers in the semiconductor and the appropriate charge's diffusivity constant, with e to ensure the correct units. Therefore, total current in the semiconductor in the presence of an electric field (from Ohm's Law) is

$$I = \sigma_p E - e D_p \nabla_r p \quad . \quad (1.3)$$

Combining equation (1.3) with (1.2) we get a current-dependent diffusion term on the left side of (1.2), since diffusion current is opposite the direction of current generated from charge injection, as outlined previously in 1.1.2

$$\frac{\partial \Delta p}{\partial t} + \frac{1}{|e|} (\nabla_r \cdot I_p) = G - \frac{\Delta p}{\tau_p} \quad . \quad (1.4)$$

From this equation, under steady-state illumination ($\frac{\partial \Delta p}{\partial t} = 0$), we can derive the hole component of current in the semiconductor which then leads us to the total current,¹⁸

$$I = I_s \left(e^{\frac{|e|V}{k_B T}} - 1 \right) - I_L \quad , \quad (1.5)$$

where

$$I_L = G |e| \sqrt{D_p \tau_p} = G |e| L_p \quad . \quad (1.6)$$

From this, it can be seen that when voltage is zero, $I = -I_L = I_{sc}$ and the system is considered to be under short circuit conditions, thus current is maximized. Conversely, V_{oc} is maximized when $I = 0$. Setting $I = 0$ in (1.5) gives us the equation for V_{oc} ,

$$V_{oc} = \frac{k_B T}{|e|} \ln \left(1 + \frac{I_L}{I_s} \right) \quad . \quad (1.7)$$

This equation also shows mathematically that it is prohibited to maximize both current and voltage at the same time in a solar cell, as stated in the previous section.

The maximum power point in a solar cell occurs when $\frac{\partial P}{\partial V} = 0$. When the voltage at maximum power (V_{mp}) is compared to V_{oc} , entropic losses are present

$$V_{mp} = V_{oc} - \frac{k_B T}{|e|} \ln \left(1 + \frac{|e| V_{mp}}{k_B T} \right) \quad . \quad (1.8)$$

These losses, in addition to losses due to charge trapping and recombination, can be explored further by looking at the dynamics of charge generation and decay.

¹⁸ For a complete derivation see ref. 2, pg. 154 (Seeger 2002).

1.2.1 Charge Transfer and Decay

The concept of charge generation was introduced in section 1.1.2 and further explored in the previous section. Since charge generation occurs on an ultrafast timescale, it is difficult to use that to explore the fundamental properties of charge generation in a material or measure characteristics such as carrier lifetime and diffusion length. Charge decay, on the other hand, can take anywhere between picoseconds and seconds depending on the material and conditions. This can be very helpful in determining how recombination is occurring in a material, where charges are migrating, and what the rate limiting step is in a charge transfer process so that a device can be improved.

Charge decay occurs on an exponential timescale. From equation (1.2) above, we can see that when light is turned off charge injection stops thus the charge generation term is removed. This is illustrated below in figure 1.7, which shows excess hole concentration in the time domain. Below the figure are equations which detail what is occurring in the semiconductor while light is on (to the left of 0 in the time domain) and when the light is turned off (to the right of 0).

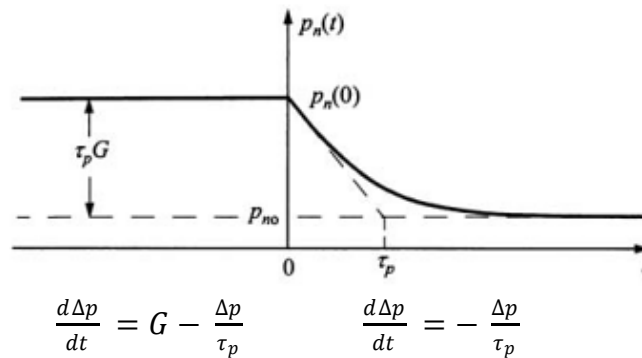


Figure 1.7 Diagram and equations illustrating charge decay as light is turned off at time $t = 0$. Diagram reproduced from ref. 3.

Solving the continuity equation in dark, we can see the exponential nature of charge decay,

$$\int_{n_0}^n \frac{1}{\Delta n} d\Delta n = - \int_0^t \frac{1}{\tau_n} dt \quad , \quad (1.9)$$

$$\ln\left(\frac{n}{n_0}\right) = -\frac{t}{\tau_n} \quad , \quad (1.10)$$

$$n = n_0 e^{-t/\tau_n} \quad . \quad (1.11)$$

Thus, from this we can see that if we plot the natural logarithm of the normalized increase in carrier density it will yield a linear relationship to time with a slope of $-\frac{1}{\tau_n}$.

Measurement of charge decay also helps to identify whether charge losses are coming from recombination or charge trapping. Deep-level traps usually serve as recombination centers since they have a high energy required to move electrons from the trap to the conduction band (and similarly holes to the valence band), thus charges are kept there for a long enough time to recombine. Shallow-level traps require less energy to release electrons to the conduction band; therefore they will keep electrons there until thermal energy frees them. This increases the chance of recombination but not as much as deep-level traps. The presence of shallow levels can be determined by looking at a photoconductivity decay plot and determining whether or not a second time constant representative of charge traps exists. Changes in temperature or quenching of charge traps with continuous white light can also be used to determine whether or not shallow levels are present.

Charges may also behave differently in PEC systems. The dynamics of a semiconductor-liquid junction are inherently different from that of a p-n junction. Charges may be trapped in surface states at the surface of the electrode, or limited by the rate of charge transfer to the electrolyte. In the case of water oxidation, the rate of hole transfer to water at the semiconductor-liquid junction plays an important role in how well a photoanode performs.

1.3 Photoanodes for Water Oxidation

The semiconductor-liquid junction at a photoanode and water behaves similarly to a p-n junction. When an n-type semiconductor and liquid electrolyte are brought into contact, electron flow occurs to equilibrate the electrochemical potential of the solution with the Fermi level of the semiconductor. The resulting electric field causes holes to diffuse to the n-type region and electrons to diffuse into the solution, resulting in an upward band bending at the photoanode-electrolyte interface (figure 1.8). Because of this there is also a small negative charge present in the Helmholtz layer of the solution, though this layer is far smaller than the depletion width of a solid semiconductor.

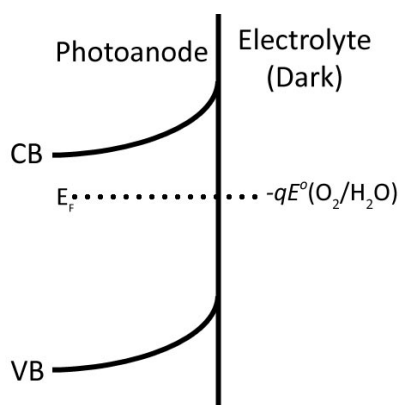


Figure 1.8 Band diagram for an n-type photoanode in contact with a water electrolyte without illumination. In this case, the photoanode has a thickness approximately equal to its depletion width.

Upon illumination, the electrochemical potentials for minority and majority carriers are separated forming a hole quasi-fermi level at the electrochemical potential of the solution and an electron quasi-fermi level that is at a specific voltage (V_{oc}) higher than the hole quasi-fermi level.

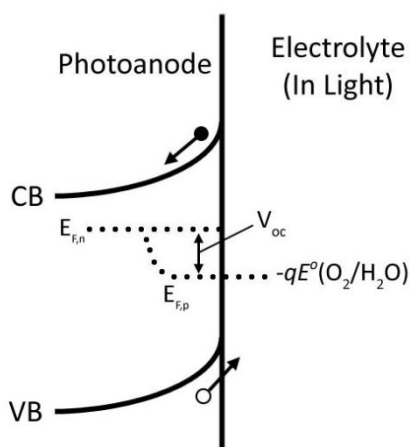


Figure 1.9 Similar band diagram as figure 1.8 except under illumination with $E_{\text{photon}} > E_g$.

Spontaneous water splitting, however, does not occur unless the semiconductor has a conduction band that lies energetically above the electrochemical potential of water reduction and a valence band that lies below that of water oxidation. Below is a comparison of many photoanode and photocathode materials showing where their conduction and valence bands lie with respect to water oxidation and reduction.¹⁹

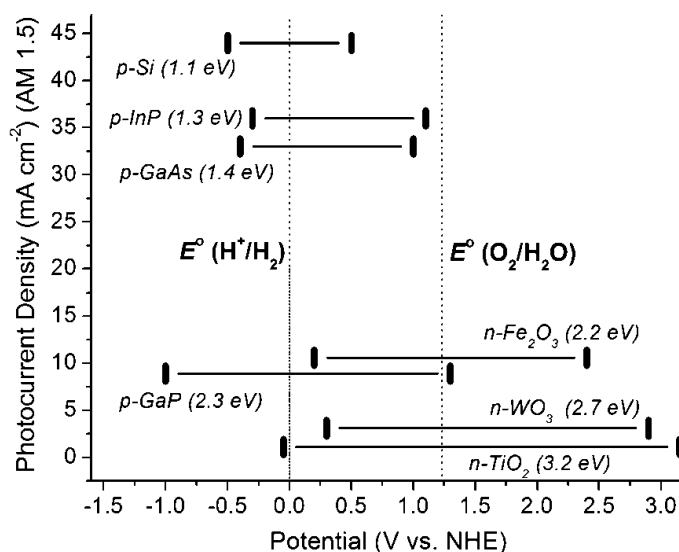


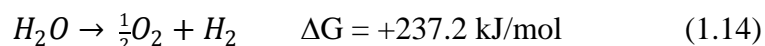
Figure 1.10 Conduction (left) and valence (right) band positions for different photoanode/cathode materials at pH 1, with band gaps in parenthesis. The y-axis indicates their maximum theoretical photocurrent under AM 1.5 illumination. Graph reproduced from [19].

¹⁹ Walter, M. G.; Warren, E. L.; McKone, J. R.; Boettcher, S. W.; Mi, Q.; Santori, E. A.; Lewis, N. S. *Chem. Rev.* **2010**, *110*, 6446

In addition to this, significant overpotentials are required to drive water oxidation and reduction. Since water oxidation is a four electron process whereas water reduction requires only two electrons, a much higher overpotential is needed for oxidation (over 400 mV at 10 mA/cm²). Still, the reduction of water to hydrogen requires around 50 mV at 10 mA/cm².²⁰ This places strict requirements on the placement of conduction and valence bands for water splitting materials.

Another requirement specific to photoanodes is resistance to corrosion. Oxidation reactions easily corrode most materials, and water oxidation is no exception. Typically only oxides can be used as photoanodes because of this; other materials would oxidize and lose their catalytic properties. Band gap is also related to stability; typically semiconductors with a higher band gap are more stable and resistant to corrosion than semiconductors with smaller band gaps. Thermodynamically, in water oxidation this is because many wide band gap semiconductors have reductive decomposition potentials that are more negative than their conduction band edge (for water reduction), and oxidative decomposition potentials more positive than their valence band edge (for water oxidation). This makes selecting photoanodes for water oxidation even more difficult, as the most stable possess a band gap so high that they do not absorb a significant amount of light from the solar spectrum (such as TiO₂).

While a high band gap offers stability and a higher V_{oc} due to low dark current and greater charge separation, for a water splitting system the material must also have a high band gap due to the free energy change required for the conversion of one molecule of water to H₂ and ½ O₂. Below are the anodic, cathodic, and combined chemical reactions undergone in water splitting:



By the relation $G = -nFE$ from chemical kinetics, this corresponds to 1.23 eV per electron transferred. Thus, the theoretical minimum band gap for a water splitting photoelectrode is 1.23 eV. Practically, a higher energy is needed due to overpotentials as mentioned previously, therefore the energy required per electron and thus minimum band gap for a photoelectrode is reported at 1.6-2.2 eV.²¹

Efficiency of sunlight to chemical energy conversion systems such as this is also handled differently than in a p-n junction photovoltaic cell. Assuming no corrosion reactions are present and the Faradaic efficiency of both water oxidation and reduction is unity, the following equation can be used to calculate efficiency:

$$\eta = \frac{J_{mp} (1.23V - V_{app})}{P_{in}} \quad (1.15)$$

²⁰ Weber, M. F.; Dignam, M. J. *J. Electrochem. Soc.* **1984**, 131, 1258.

²¹ Bolton, J. R.; Strickler, S. J.; Connolly, J. S. *Nature* **1985**, 316, 495.

where J_{mp} is the current density at the maximum power point, V_{app} is the applied voltage, and P_{in} is illumination power density. A two electrode measurement configuration must be used to determine maximum photocurrent density. When using this calculation with a potentiostat and three-electrode configuration, polarization losses associated with driving the water reduction reaction at the counter electrode are not taken into account.¹⁹ In addition, V_{app} may slightly exceed the bias voltage measured since the measured voltage is a combination of V_{app} and $V_{a,oc}$, the open circuit anodic potential measured with respect to the reference electrode.²² These can yield exaggerations in measured photocurrent. This equation also assumes that reverse reactions, such as reduction of O_2 at the cathode, are suppressed.

1.3.1 Processes at the Electrode Surface

In a photoanode, the driving force of hole transfer to the solution is provided by band bending at the interface and the overpotential from the semiconductor's valence band edge to the water oxidation potential. Similar to p-n junction photovoltaic cells, we want to ensure that the photoanode's Fermi level is much higher in energy than the chemical potential of the water oxidation reaction to maximize open circuit voltage and maximize that driving force. pH also plays a crucial role in optimizing hole transfer to solution.

The effect of pH on electrochemical reactions is governed by the Nernst equation:

$$E = E^o - \frac{RT}{nF} \ln \frac{[Red]}{[Ox]} \quad (1.16)$$

Applying this to the water oxidation reaction, we get the following relation:

$$E^o(O_2/H_2O) = 1.23 V - 0.059 V \times pH \text{ vs. NHE} \quad (1.17)$$

As pH changes, however, protonation and deprotonation of surface hydroxyl groups, changes in surface energetics, and surface dipole effects due to the negative charge present in the Helmholtz layer make the effect of pH on a photoanode's surface much more complex.²³ Partially due to this, the actual mechanism of hole transfer to water at a photoanode is multi-step and not fully understood.²⁴

1.4 Goals of this Study

This study demonstrates new approaches to synthesizing and understanding photoanodes for water splitting. The goals of this study are to synthesize new, high efficiency photoanodes for water oxidation and understand their underlying mechanisms. A secondary goal of this study is to use materials that are Earth abundant so that this approach can have a broader impact after this initial proof of concept.

²² Varghese, O. K.; Grimes, C. A. *Sol. Energy Mater. Sol. Cells* **2008**, 92, 374.

²³ Gerischer, H. *Electrochimica Acta* **1989**, 34, 1005.

²⁴ Hamann, T. W.; Gstrein, F.; Brunschwig, B. S.; Lewis, N. S. *Chem. Phys.* **2006**, 326, 15.

With the hypothesis that we can use heteronanostructure architecture to simultaneously improve light absorption and charge separation and transport in common photoanode materials by decoupling the path of light absorption with the path of charge separation, we can realize this goal. By orthogonalizing the path of light, light will be fully absorbed by a thin, conformal film of photocatalyst that is close in thickness to the diffusion length of charge carriers in the film's material. This will give us the charge transport properties of a thin photoactive material and the absorptive properties of a thicker material. In addition to this, the higher surface area inherent in nanostructures should result in more catalytically active sites per macroscopic unit area of the material. To further prove this hypothesis, this heterostructure approach is used to improve the photocatalytic efficiency of tungsten oxide coated on porous silica particles, in addition to the nanonet study.

In order to prove that charge transport is optimized in the films coated on nanostructures, photoconductivity decay measured on the microsecond timescale by time-resolved microwave conductivity (TRMC) will be used. This method can also be used to probe the semiconductor-liquid junction at a photoanode and shed new light on the water oxidation reaction. In addition to this, we will show changes in charge transport on the surface of photoanodes as they are interfaced with an electrolyte.

Additional References

The following textbooks were used as primary references in this chapter:

1. Atkins, P.; De Paula, J. *Physical Chemistry*, 8th ed.; W. H. Freeman and Company: New York, 2006.
2. Seeger, K. *Semiconductor Physics: An Introduction*, 8th ed.; Springer-Verlag: Berlin, Germany, 2002.
3. Sze, S. M. *Physics of Semiconductor Devices*, 2nd ed.; John Wiley & Sons, Inc.: New York, 1981.
4. Kittel, C. *Introduction to Solid State Physics*, 8th ed.; John Wiley & Sons, Inc.: New York, 2005.
5. West, A. R. *Basic Solid State Chemistry*, 2nd ed.; John Wiley & Sons, Inc.; New York, 1999.
6. Archer, M. D. *Clean Electricity from Photovoltaics*, Imperial College Press: London, 2001.
7. Finklea, H. A. *Semiconductor Electrodes*, Elsevier: Amsterdam, 1998.
8. Fonash, S. J. *Solar Cell Device Physics*, 2nd ed.; Academic Press: Burlington, MA, USA, 2010.
9. Goetzberger, A.; Hoffman, V. U. *Photovoltaic Solar Energy Generation*, Springer-Verlag: Berlin, Germany, 2005.

Chapter 2

Materials and Methods

2.1 Synthesis and Characterization Techniques

2.1.1 Atomic Layer Deposition

Atomic Layer Deposition (ALD) is a variant of chemical vapor deposition (CVD) that synthesizes thin films one atomic layer at a time. Typically, ALD breaks a CVD reaction into two half reactions that occur separately during the reaction. This ensures the precursors that may be extremely reactive remain separated throughout the reaction. One pulse of each precursor, which in theory would produce a single atomic layer of a compound, is generally referred to as a cycle. Since the film is grown in a layer-by-layer fashion, atomic level thickness control of the film can be obtained.

Below is an illustration of this process with common ALD precursors, trimethylaluminum (TMA) and water. This is used to grow an Al_2O_3 thin film on a hydrophilic surface (e.g. one terminated by hydroxyl groups).

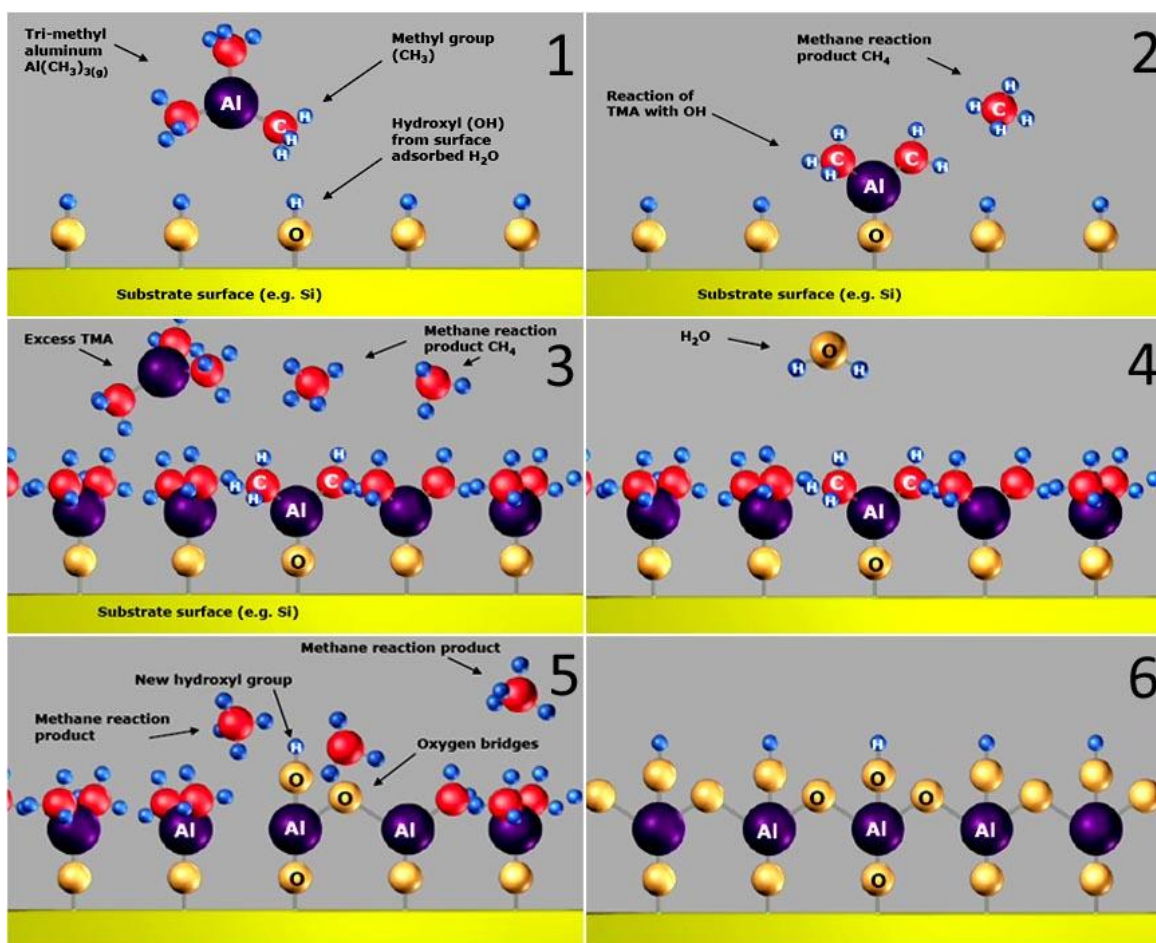


Figure 2.1 Illustration of one cycle in the atomic layer deposition process for aluminum oxide in six steps. Reproduced from www.cambridgenanotech.com.

True ALD growth processes have three features that distinguish them from CVD growths. First, there is a linear and reproducible relationship between film thickness and number of ALD growth cycles. This is a consequence of the sequential layer-by-layer nature of ALD, and allows for atomic layer precision in thickness control. Second is the self-limiting aspect of each precursor pulse. ALD precursors do not react with each other, therefore when they react with species on a solid surface that active site is occupied, leading to saturation in chemisorption for each precursor. This can be demonstrated by holding all growth parameters constant except for precursor dose and demonstrating that film thickness increases according to a Langmuir isotherm as dose of precursor is increased; that is, it tapers off at a specific point where surface adsorption is maximized.

A consequence of this and the third feature of ALD growths is high step coverage. As one can imagine with the steps outlined in figure 2.1, these films will coat hydrophilic surfaces (or any surface which is compatible with the chosen precursors) uniformly and conformally. This can be especially advantageous for coating thin films on nanostructures, as is demonstrated in this study. This feature can be evaluated by directly looking at the thin film under a transmission electron microscope (TEM).

After ALD growth, the next important step is characterizing the thin film and determining what can be done in order to optimize it for its chosen application. Frequently, films that are grown by ALD use temperatures less than 350°C which necessitates high temperature annealing to achieve the desired crystal structure and/or oxidation state. Methods such as TEM, x-ray diffraction (XRD), and x-ray photoelectron spectroscopy (XPS) can be used to evaluate this.

2.1.2 Solid State Characterization

In this study, eight typical methods of characterizing solid samples were used: electron microscopy (TEM and SEM), selected area electron diffraction (SAED), XRD, XPS, energy-dispersive x-ray spectroscopy (EDX), spectroscopic ellipsometry, and absorption spectroscopy. TEM, SEM, XRD, SAED, and ellipsometry were used in conjunction to determine the atomic structure of grown thin films and heteronanostructures and their morphology on the nanoscale. XPS was used to determine the oxidation state of metals in the films to further investigate the effectiveness of annealing at different annealing conditions, and absorption spectroscopy was used to evaluate materials to determine band gap and get an idea of how effectively materials would absorb solar light.

Electron microscopes operate similarly to optical microscopes; however instead of using light with visible wavelengths as a probe they use electrons which have a wavelength determined by the de Broglie equation,

$$\lambda = \frac{h}{p} = \frac{h}{\sqrt{2mE}} . \quad (2.1)$$

Where E is kinetic energy and m is the mass of the electron. Typically a TEM will operate with 200 kV accelerating voltage, this corresponds to a wavelength of 2.5 pm. Visualizing materials on this length scale allows us to look directly at the positions of atoms in the crystal lattice and relate this data to that gained from diffraction based studies such as SAED and XRD. As implied by their names, TEM operates by imaging electrons that are transmitted through the sample while SEM detects reflected electrons in a more similar manner to the way photons are detected in optical microscopy. A TEM is also used to perform SAED, when the electron beam is focused on a spot in the crystal lattice of a sample atoms in the crystal serve as a diffraction grating, forming a pattern of destructive and constructive interference which is a reflection of the reciprocal lattice of the crystal. From the reciprocal lattice crystallographic planes can be identified and correlated to high resolution TEM (HRTEM) and XRD data. Bragg's law, on the other hand, governs XRD which images the reciprocal lattice of a crystal using reflection of x-rays, instead of transmission of electrons as in the case of SAED.

While TEM, SEM, SAED, and XRD are used to analyze the structure of a material, XPS and EDX are spectroscopic methods of elemental analysis. XPS uses high energy monochromatic x-ray radiation to eject inner shell electrons from samples via the photoelectric effect (figure 2.2). A detector then measures the kinetic energy (KE) of these electrons from which the electron's binding energy (BE) can be found by the relation,

$$BE = E_{\text{photon}} - (KE + \phi) . \quad (2.2)$$

Where ϕ is the work function of the spectrophotometer, which is constant for each instrument. Since electrons from atoms of different elements and oxidation states have distinct binding energies, both the chemical composition and oxidation state can be determined from XPS spectra. Since the KE of electrons must be conserved in XPS electron collisions must be kept to a minimum, thus an ultra-high vacuum system and sensitive instrumentation are necessary. In addition, XPS only measures the topmost atomic layers of a sample because of the low penetration depth of high energy photons.

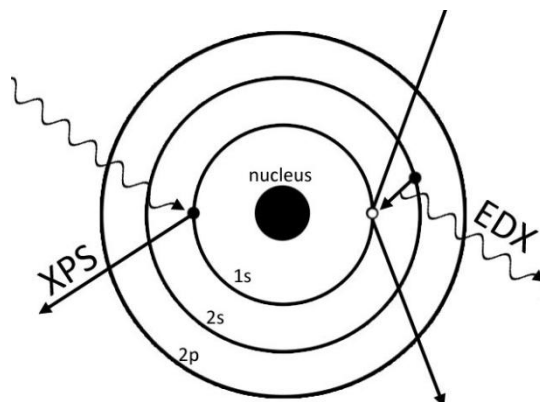


Figure 2.2 Diagram of atomic orbitals depicting a highly simplified model of processes for emission of detected particles in EDX and XPS.

EDX does not have as stringent instrumentation requirements, can perform elemental analysis that reaches spatially deeper into samples, and is generally done in an electron microscope which makes this technique more appealing. One downfall of EDX, however, is that it cannot reliably measure oxidation state. EDX uses an electron beam to eject inner shell electrons from a sample, which then causes higher energy electrons to relax to the inner shell. This emits x-rays characteristic of the energy difference between the higher energy electron's energy level and the inner shell energy level (figure 2.2). Since each element possesses different atomic structure, the energy of these x-rays will be different from element to element and can be used to identify the composition of a material.

Spectroscopic ellipsometry is an indirect technique used to measure dielectric properties of thin films. This is done by measuring the change in light polarization caused by reflection or transmission through the material. From these dielectric properties, we can determine refractive index, film thickness, and dielectric function. In an ellipsometer, polychromatic light is shined through a monochromator then a polarizer so that the light incident on the sample is monochromatic and linearly polarized. Upon reaching the film, the linearly polarized light will be scattered and absorbed based on the dielectric constant and absorbance of the film, respectively. Scattering will cause the light to become elliptically polarized, while absorption will cause less light reflected/transmitted to the detector.

In ellipsometry, the detector serves to measure both the intensity of light after interaction with the sample and the characteristics of its polarization, such as the polarization angle and amplitudes of light oscillation parallel and perpendicular to the plane of incidence. From this data we can find the complex reflectance ratio for a sample at each wavelength, which can be

fitted to different theoretical models²⁵ to determine dielectric constant, film thickness, and refractive index of the material.

Absorption spectroscopy is the most common of all the methods mentioned here. Monochromatic light is shined through a sample to a detector that measures the intensity of the transmitted light at each wavelength. An integrating sphere can also be used to compensate for reflection and scattering. One uncommon approach that is used in this study is application of the Tauc equation²⁶ to absorption spectra in order to determine a material's band gap,

$$(\alpha hv)^{1/2} = k(hv - E_g) . \quad 2.3$$

Where α is the material's absorption coefficient, hv is photon energy, and k is an arbitrary constant. The above equation holds true for indirect band gap semiconductors in the UV/visible region, for direct band gap semiconductors in this region the term on the left is $(\alpha hv)^2$. Examples of this method can be seen throughout chapter 3 where the equation was plotted out then extrapolation was used in order to accurately determine the band gap of the three different materials synthesized.

While solid state characterization methods can be used to determine key characteristics of the materials synthesized, determination of efficiency and photoelectrochemical properties are just as important if not more so. In addition to determining how effectively a PEC cell converts sunlight to chemical energy, PEC methods can be used to probe the semiconductor-liquid junction and measure properties outlined in chapter 1 such as V_{oc} , J_{sc} , and FF. From these, we can find out what aspects of the solar cell still need improvement.

2.1.3 PEC Characterization

Most central to a study on improving the efficiency of photoanode materials is the manner in which efficiency is determined. Methods that are used in this study include I-V analysis, measurement of device efficiency, and measurement of quantum efficiency. Section 1.3 covers efficiency determination and considerations for two-electrode and three-electrode systems, therefore this material will not be covered here. The properties of I-V curves, such as how to determine V_{oc} , I_{sc} , and FF, have also been covered previously in 1.1.2. This section will then cover how to measure both internal and external quantum efficiency.

In a solar cell, external quantum efficiency is the ratio of the number of charge carriers collected to the number of photons incident on the solar cell at specific wavelengths varied over the absorbance of the solar cell. This is also known as incident photon to electron conversion efficiency (IPCE). Wavelength is generally varied throughout the UV and visible regions when measured for a water-splitting system, since photon energy must be in the range of 1.6 – 2.2 eV in order to split water.²⁷ This measurement is done in two-electrode configuration usually with a bias on the photoanode. Photocurrent density is then related to IPCE by the following equation,

²⁵ The Cauchy equation is typically used as a theoretical model for visible light spectroscopic ellipsometry. For the UV and IR regions of the electromagnetic spectrum, the Sellmeier equation is more accurate. Sellmeier, W. *Annalen der Physik und Chemie* **1871**, 219, 272.

²⁶ Mott, N. F.; Davies, E. A. *Electronic Processes in Non-Crystalline Materials*, Oxford University Press: Oxford, UK, 1979

²⁷ Bolton, J. R.; Strickler, S. J.; Connolly, J. S. *Nature* **1985**, 316, 495.

$$IPCE = 1240 \frac{I_p(\lambda)}{P(\lambda)\lambda} \quad (2.4)$$

Where $I_p(\lambda)$ is photocurrent density at wavelength λ and $P(\lambda)$ is incident light power.²⁸

Likewise, internal quantum efficiency is the ratio of number of charge carriers collected to the number of photons absorbed by the solar cell. This is known as absorbed photon to electron conversion efficiency (APCE). This is a more direct measure of recombination, charge separation, and charge transfer efficiency in the solar cell's photoactive material than IPCE, which also taken into account transmission, reflection, and other absorption losses. APCE is determined by dividing IPCE by light-harvesting efficiency (LHE),²⁹

$$APCE = IPCE/LHE = IPCE/1 - 10^{-Abs} \quad (2.5)$$

APCE can be increased by decreasing recombination in the solar cell and improving charge dynamics overall. In order to determine how to do this effectively a more thorough knowledge of charge separation and transfer in the material is needed though. This leads us to explore methods of measuring charge recombination and lifetime.

2.1.4 Time-Resolved Microwave Conductivity (TRMC)

TRMC is a contactless, non-destructive method of measuring carrier lifetime in semiconductors.³⁰ When a semiconductor is irradiated with microwaves, electrons in the material's conduction band resonate with the same frequency as the microwaves while electrons in the valence band are unaffected. This has a scattering effect which is in essence the same as reflection at optical wavelengths. Reflection of the microwaves is also efficient and in proportion to the concentration of electrons in the conduction band.³¹ This allows us to explore the amount of time carriers are present in the conduction band on the time scale of one microwave oscillation, which is typically in the nanosecond range. This is ideal for measuring photoconductivity decay and carrier lifetime (section 1.2.1) for materials with carrier lifetimes in the tens of nanoseconds or higher.

This study uses a home built 20 GHz TRMC measurement system for carrier lifetime measurements. This corresponds to a theoretical time constant of 2 ns (the time it takes for one full oscillation of 20 GHz electromagnetic waves), though practically the time constant is approximately 20 ns due to non-idealities in the system which are discussed later. The TRMC system consists of four major parts: a pulsed excitation source, a microwave source including waveguide to transport the microwaves, a detection system, and a sample cavity.

²⁸ Varghese, O. K.; Grimes, C. A. *Sol. Energy Mater. Sol. Cells* **2008**, 92, 374.

²⁹ Sambur, J. B.; Novet, T.; Parkinson, B. A. *Science* **2010** 330, 63.

³⁰ Kunst, M.; Beck, G. *J. Appl. Phys.* **1986**, 60, 3558.

³¹ De Haas, M. P.; Warman, J. M. *Chem. Phys.* **1982**, 73, 35.

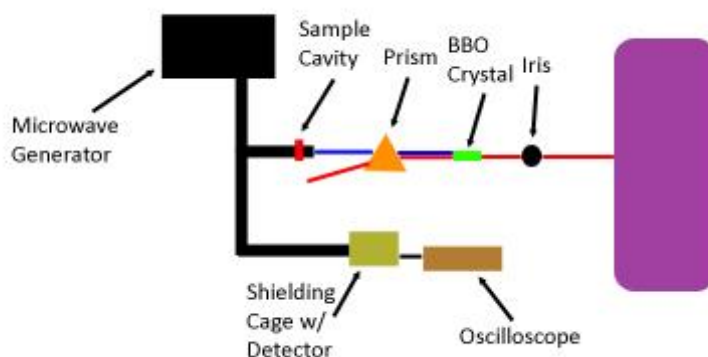


Figure 2.3 Color-coded schematic of the TRMC system described in this study showing all four primary components. The excitation in this case is the second harmonic of a pulsed 775 nm laser though it is interchangeable with a pulsed xenon flashlamp when different timescales are explored.

In this study, two different excitation sources were used. A 388 nm wavelength light with a 400 fs pulse width and 1 ms between pulses was generated with a nonlinear optic crystal (β -barium borate, Castech) in the path of a 775 nm laser (CPA-2010, Clark-MXR Inc.) as shown above. This was used to measure photoconductivity decay in the sub-microsecond regime. For longer decays a simpler system was employed using a pulsed Xe flashlamp which also afforded lower noise in measurements due to its power source producing less electrical interference. The Xe flashlamp has a FWHM of $\sim 1.3 \mu\text{s}$ (figure 2.4), which when interpreted in a logarithmic form allows for reliable and reproducible carrier lifetime measurement in the range of 0.5-0.8 μs and higher. It also excites samples using a broad spectrum of light which eliminates the need for wavelength selectivity as in laser measurements and allows for the release of thermally trapped carriers in materials, though it may also introduce above band gap excitation that can further complicate results.

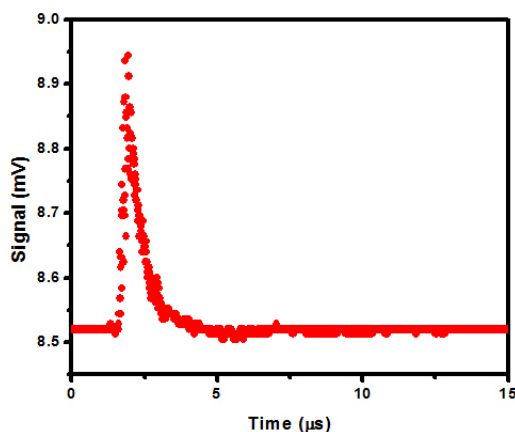


Figure 2.4 Iron oxide (dry) photoconductivity decay measured by the Xe flashlamp. Since iron oxide has a carrier lifetime far below its detection limit, this data shows the pulse characteristics of the lamp.

Rectangular WR-42 waveguide (K-band, 0.420 x 0.170 in, Waveline Inc.) was used to transport the microwaves from a microwave source (HP 8350B Sweep Oscillator with HP

83570A plug-in attenuation module) to a 20 GHz, 200 MHz bandwidth circulator (JCWR42-24, JQL Electronics). From the circulator the microwaves reached the sample cavity, where they were reflected back through the circulator, through additional waveguide, and to a detector system. The reflected microwaves were detected by a Schottky diode (Advanced Control Devices ACS2644NZ, rise time <1ns, 50 Ω impedance) which was encased along with excess coaxial cable in a solid copper faraday cage (1 mm thick). This was connected to a Tektronix TDS 2022B oscilloscope which displayed the data. Low signal measurements were also performed with a preamplifier (Stanford Research Systems, SR445A 350 MHz).

The K-band microwave cavity is a standard reflection cavity machined from copper (figure 2.5). Apertures on the front and back are the size of WR-42 waveguide, with a large open space for samples in the center and a side hole for electrolyte drainage.

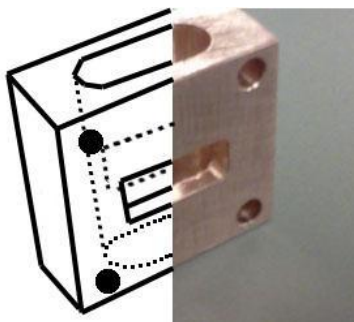


Figure 2.5 K-band sample cavity overlaid with a wire diagram.

Since the cavity is by necessity larger than the waveguide in order to hold samples securely, unwanted attenuation of the microwave signal at the cavity causes a slight loss in intensity, to which can be attributed most of the difference between the theoretical time constant for 20 GHz microwaves (2 ns) and the practical time constant of the system (20 ns). After the cavity, waveguide is terminated by a silver wire grid parallel to the short side of the waveguide.

2.2 Materials

2.2.1 Tungsten Trioxide

WO₃ has been studied as a photoelectrode since its photocatalytic properties were discovered in 1976.^{32,33} Due to its band gap at 2.5-2.8 eV,³⁴ it can offer higher conversion efficiency in PEC cells than TiO₂ by absorbing more of the solar spectrum. Significant drawbacks however have prevented WO₃ from realizing its potential, including its poor stability in pH 7 water and lower IPCE than TiO₂.^{35,36} Many different strategies to improve the stability

³² Hodes, G.; Manassen, D. C. J. *Nature* **1976**, 260, 312.

³³ Butler, M. A. *J. Appl. Phys.* **1977**, 48, 1914.

³⁴ Cole, B.; Marsen, B.; Miller, E.; Yan, Y.; To, B.; Jones, K.; Al-Jassim, M. *J. Phys. Chem. C* **2008**, 112, 5213.

³⁵ Liu, R.; Lin, Y.; Chou, L. Y.; Sheehan, S. W.; He, W.; Zhang, F.; Hou, H.; Wang, D. *Angew. Chem. Int. Ed.* 2011, 50, 499.

and efficiency of WO_3 have been tried, including tuning morphology,^{37,38} doping,³⁹ and introduction of surface catalysts.⁴⁰ Currently, the highest photocurrent attained with a WO_3 photoanode uses an embedded silver plasmonic nanostructure in $1 \mu\text{m}$ WO_3 to achieve 2.1 mA/cm^2 at 0.9 V vs. RHE in a $1 \text{ M H}_2\text{SO}_4$ electrolyte.⁴¹

Many different synthesis methods have been used to produce WO_3 thin films and nanostructures. Solution deposition has been employed to in thin film⁴² and nanostructure synthesis,⁴³ while CVD⁴⁴ and ALD⁴⁵ have also been used. Of these methods, ALD is the most versatile due to the high step coverage and precise thickness control of ALD grown films. Prior to the study reported in chapter 3 however, no method of growing WO_3 by ALD existed without the presence of byproducts reactive to most substrates such as HF.⁴⁶

WO_3 also has a crystal structure that allows the insertion of small cations such as H^+ and Li^+ . The result of this is a change in oxidation state of tungsten which in turn changes the color of the film, making WO_3 useful in a variety of electrochromic applications.⁴⁷ Briefly, we discovered that under-oxidized WO_3 with low crystallinity (as-grown by the ALD without post-growth annealing) exhibited fast switching where it rapidly changed colors as cations were inserted into and removed from the crystal lattice faster than stoichiometric, monoclinic WO_3 obtained after post-growth annealing at 550°C (section 3.1.2).

The studies described in chapters 3 and 4 incorporate WO_3 into heterostructures. When grown on TiSi_2 nanonets, efficiency is increased due to an increased path length of light absorption orthogonal to the path of charge separation through the film. A manganese complex, when applied to the film, helps to improve stability enabling a WO_3 thin film photoanode to split water in a pH 7 environment. Finally, silica gel particles are used to provide a transparent and lightweight scaffold and increase the amount of photocatalytic surface area of the film that is in contact with solution.

2.2.2 Iron Oxide

$\alpha\text{-Fe}_2\text{O}_3$, or hematite, has recently been recognized for water splitting applications due to its high stability and wide absorption spectrum which extends farther into the visible light region than WO_3 . It also contains two of the most abundant elements on earth, iron and oxygen, which makes it even more promising as a widespread photocatalyst. Hematite has a band gap between 2.0 and 2.2 eV ,⁴⁸ giving it the potential to absorb more of the solar spectrum than either of the

³⁶ Santato, C.; Ulmann, M.; Augustynski, J. *J. Phys. Chem. B* **2001**, 105, 936.

³⁷ Santato, C.; Odziemkowski, M.; Ulmann, M.; Augustynski, J. *J. Am. Chem. Soc.* **2001**, 123, 10639.

³⁸ Kim, J. K.; Shin, K.; Cho, S. M.; Lee, T. W.; Park, J. H. *Energy Environ. Sci.*, **2011**, 4, 1465.

³⁹ Solarska, R.; Alexander, B. D.; Braun, A.; Jurczakowski, R.; Fortunato, G.; Stiefel, M.; Graule, T.; Augustynski, J. *Electrochim. Acta* **2010**, 55, 7780.

⁴⁰ Kim, J.; Lee, C. W.; Choi, W. *Environ. Sci. Technol.* **2010**, 44, 6849.

⁴¹ Solarska, R.; Krolikowska, A.; Augustynski, J. *Angew. Chem. Int. Ed.* **2010**, 49, 7980.

⁴² Pauporte, T. *J. Electrochem. Soc.* **2002**, 149, C539.

⁴³ Su, J.; Feng, X.; Sloppy, J. D.; Guo, L.; Grimes, C. A. *Nano Lett.* **2011**, 11, 203

⁴⁴ Meda, L.; Breilkopf, R. C.; Haas, T. E.; Kirss, R. U. *Thin Solid Films* **2002**, 402, 126.

⁴⁵ Tagtstrom, P.; Martensson, P.; Jansson, U.; Carlsson, J. O. *J. Electrochem. Soc.* **1999**, 146, 3139.

⁴⁶ Herrera, J. E.; Kwak, J. H.; Hu, J. Z.; Wang, Y. F.; Peden, C. H. F.; Macht, J.; Iglesia, E. *J. Catal.* **2006**, 239, 200.

⁴⁷ Niklasson, G. A.; Granqvist, C. G. *J. Mater. Chem.* **2007**, 17, 127.

⁴⁸ Kennedy, J. H.; Frese, J. *J. Electrochem. Soc.* **1978**, 125, 709–714.

two other catalysts studied and is one of the few materials that has a band gap this small yet still has a valence band negative enough to provide the overpotential required by the water oxidation reaction.⁴⁹ Its carrier diffusion distance and lifetime, however, are extremely short; several orders of magnitude shorter than in TiO₂ and WO₃.⁵⁰ This is further complicated by hematite's low absorption coefficient, which makes charge transport a major hurdle to overcome if a practical hematite photoanode is to be realized.

Because of the low absorption coefficient and short charge diffusion length in hematite, ultrathin films and nanostructures seem promising.⁵¹ Photocurrents up to 3.0 mA/cm² at 1.23 V vs. RHE have been seen when nanostructured hematite is doped with silicon to increase conductivity and decorated with an oxygen evolving catalyst.⁵² Hematite is also a more complicated crystal system than WO₃ or TiO₂, which can cause difficulties when studying it due to the introduction of charge traps and defect states.⁵³ Charge transfer in hematite systems can be highly dependent on the environment; deep level traps can be influenced by changes in temperature, as can reaction kinetics at its surface.⁵⁴ Exploring charge transfer in iron oxide photoanodes has come to attention recently and is studied further in chapter 5.

2.2.3 Titanium Dioxide

The first water splitting photoanode discovered and most common photoanode material in dye-sensitized solar cells is anatase TiO₂, though it is explored only briefly in this study. Titanium dioxide has a variety of applications ranging from paint pigment to food coloring. Since it is widespread and safe, solar cells (specifically DSSCs) using TiO₂ are already in circulation; however in this study we are only interested in its properties with respect to water splitting. Due to its wide band gap at 3.2 eV,⁵⁵ TiO₂ has an impressive chemical stability and a conduction and valence band that straddle the water oxidation and reduction potentials, though due to the overpotential required at water reduction it is incapable of unassisted water splitting (i.e. without an external bias). Its anatase phase has a lower transition temperature than monoclinic WO₃ does too, making it easier to synthesize. However, its high band gap and low carrier density severely limit its absorption and conductivity.

In terms of synthesis, many methods of growing thin films and nanostructures are commonplace in DSSCs and can be extended to photosynthetic PEC cells. Of these, synthesizing nanostructures out of TiO₂⁵⁶ and doping with different transition metals⁵⁷ have been promising approaches. Nanostructures can be used to increase catalytic sites by increasing surface area and to simultaneously improve light absorption and charge separation as described previously. Doping, on the other hand, can be used to modify the carrier density and/or band gap of TiO₂. In

⁴⁹ Dare-Edwards, M.; Goodenough, J.; Hamnett, A.; Trelvellick, P. *J. Chem. Soc., Faraday Trans. 1* **1983**, 79, 2027.

⁵⁰ Mohapatra, S. K.; John, S. E.; Subarna, B.; Misra, M. *Chem. Mater.* **2009**, 21, 3048.

⁵¹ Formal, F. L.; Gratzel, M.; Sivula, K. *Adv. Funct. Mater.* **2010**, 20, 1099.

⁵² Tilley, S. D.; Cornuz, M.; Sivula, K.; Gratzel, M. *Angew. Chem. Int. Ed.* **2010**, 49, 6405.

⁵³ Pendlebury, S. R.; Barroso, M.; Cowan, A. J.; Sivula, K.; Tang, J.; Gratzel, M.; Klug, D.; Durrant, J. R. *Chem. Comm.* **2011**, 47, 716.

⁵⁴ Cowan, A. J.; Barnett, C. J.; Pendlebury, S. R.; Barroso, M.; Sivula, K.; Gratzel, M.; Durrant, J. R.; Klug, D. R. *J. Am. Chem. Soc.* **2011**, Article ASAP

⁵⁵ Kay, A.; Cesar, I.; Gratzel, M. *J. Am. Chem. Soc.* **2006**, 128, 15714.

⁵⁶ Grimes, C. A. *J. Mater. Chem.* **2007**, 17, 1451.

⁵⁷ Bak, T.; Nowotny, J.; Rekas, M.; Sorrell, C. C. *Int. J. Hydrogen Energy* **2002**, 27, 991.

some cases titanium 3d orbitals mix with the d orbitals of the dopant,⁵⁸ alternatively a larger dopant atom can physically distort the anatase crystal lattice of TiO₂ to reduce its band gap.⁵⁹ One such method of reducing the band gap of TiO₂ through doping with tungsten is demonstrated in section 3.2.

Additional References

The following textbooks were used as primary references in this chapter:

1. Seeger, K. *Semiconductor Physics: An Introduction*, 8th ed.; Springer-Verlag: Berlin, Germany, 2002.
2. Sze, S. M. *Physics of Semiconductor Devices*, 2nd ed.; John Wiley & Sons, Inc.: New York, 1981.
3. West, A. R. *Basic Solid State Chemistry*, 2nd ed.; John Wiley & Sons, Inc.; New York, 1999.

⁵⁸ Yamashita, H.; Harada, M.; Misaka, J. Takeuchi, M.; Ichihashi, Y.; Goto, F.; Ishida, M.; Sasaki, T.; Anpo, M. *J. Synchrotron Radiat.* **2001**, 8, 569.

⁵⁹ Ghicov, A.; Yamamoto, M.; Schmuki, P. *Angew. Chem. Int. Ed.* **2008**, 47, 7934.

Chapter 3

ALD Synthesis and Characterization of WO_3 , Fe_2O_3 , and $\text{Ti}_{0.7}\text{W}_{0.3}\text{O}_2$ Thin Films

3.1 Synthesis of WO_3 Thin Film

The heteronanostructures used for water splitting in this study consist of two separate components: a conductive nanonet core which acts as a high surface area scaffold to improve absorption and electron transport, and a crystalline photocatalytic film that is of comparable thickness to the diffusion length of charges to prevent recombination. In addition to this, the film should completely cover the nanonet core and be thinner than the material's depletion width when interfaced with an electrolyte. These strict design requirements call for a high degree of control over thickness and step coverage (conformality) in the thin films' synthesis, something that can be afforded by ALD more so than any other synthesis method. While nanonet growth and characterization is described elsewhere,^{60,61} this chapter covers the methods used to synthesize crystalline, photocatalytic thin films of WO_3 , Fe_2O_3 , and $\text{Ti}_{0.7}\text{W}_{0.3}\text{O}_2$ to be used as the photoactive material in heteronanostructures.

3.1.1 High and Low Growth Rate Synthesis

Previous methods of growing WO_3 by ALD were achieved using WF_6 and water as precursors. While this was successful, one of the byproducts of the reaction between WF_6 and water is HF, which damages most substrates including silicon containing compounds. In order to facilitate WO_3 growth on TiSi_2 , we developed a new method of WO_3 ALD. Instead of using WF_6 , a tungsten amide compound used first by Becker et al in the synthesis of WN thin films⁶² was employed with water as an oxidant. Preliminary tests of this new growth method included

⁶⁰ Zhou, S.; Liu, X.; Lin, Y.; Wang, D. *Angew. Chem. Int. Ed.* **2008**, 47, 7681.

⁶¹ Zhou, S.; Liu, X.; Lin, Y.; Wang, D. *Chem. Mater.* **2009**, 21, 1023.

⁶² Becker, J. S.; Suh, S.; Wang, S.; Gordon, R. G. *Chem. Mater.* **2003**, 15, 2969.

depositing WO₃ thin films on n-Si(100) and fluorine-doped tin oxide (FTO) by alternating the exposure of (tBuN)₂(Me₂N)₂W (Sigma Aldrich, 97%) and deionized water at 350°C in a Savannah 100 ALD system (Cambridge Nanotech). Precursor pulse times were varied until the optimum growth conditions were discovered (table 1).

ALD operation	(tBuN) ₂ (Me ₂ N) ₂ W pulse	N ₂ purge	H ₂ O pulse	N ₂ flow ('stopvalve')	N ₂ purge
Time (s)	2s	10s	0.05s	5s	10s

Table 3.1 One ALD cycle for WO₃ growth with a growth rate of 1.01Å/cycle.

In this study, 'stopvalve' is defined as when exhaust valve of the ALD system is closed allowing for longer precursor exposure to the substrate. While optimum temperatures were found to be 350°C for the substrate, 75°C for (tBuN)₂(Me₂N)₂W (due to its low vapor pressure of 0.37 torr at 30 °C), and 25°C for H₂O (room temperature) with N₂ flowing throughout the growth at 10 sccm. Growths were performed successfully with these parameters for over 2000 cycles.

A typical ALD process exhibits three major growth characteristics; this includes a linear relationship between film thickness and number of deposition cycles, self-limiting adsorption of precursors, and high step coverage. Figure 3.1 shows that the growth is self limiting for both precursors (1a and 1b) and has a very linear increase in film thickness as deposition cycles increase (d).⁶³

⁶³ Liu, R.; Lin, Y.; Chou, L. Y.; Sheehan, S. W.; He, W.; Zhang, F.; Hou, H.; Wang, D. *Angew. Chem. Int. Ed.* **2011**, 50, 499.

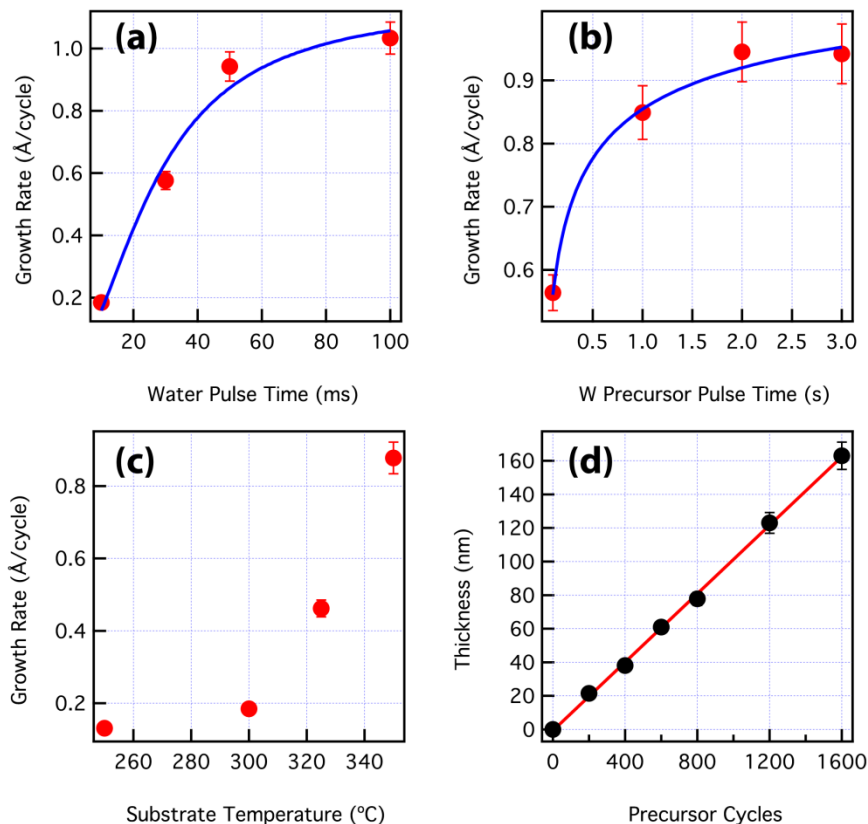


Figure 3.1 WO_3 growth characteristics that demonstrate the growth falls in the ALD regime. (a) and (b) show that the growth is self-limiting and are fitted to the Langmuir adsorption model (eq. 3.1). (c) shows the growth's sensitivity to substrate temperature, and (d) demonstrates a linear relationship between film thickness and number of cycles. Reproduced from [63].

As seen in 1a and 1b, the growth rate begins to saturate after the pulse times of water and $(^tBuN)_2(Me_2N)_2W$ reach 0.05s and 2.0s, respectively. The position of the points of saturation depends on both the rate of adsorption and rate of precursor reaction. Assuming that adsorption and reaction of precursors is uniform throughout the substrate, the Langmuir adsorption model was applied to relate the growth rate with the dose of precursor,⁶⁴

$$\theta = \frac{\alpha\mu}{1 + \alpha\mu} \quad (3.1)$$

Where θ is the amount of gas adsorbed, α is a constant, and μ is the concentration of gaseous precursor molecules and is proportional to pressure.

One peculiar aspect of this growth is the necessity for a large dose of water; the growth of the film was hindered significantly at lower exposure times for water. With only a 0.05s water precursor pulse (i.e. without the 5s of water exposure afterwards) the film cannot exceed ~12 nm in thickness. After looking into the basic chemistry of the precursor by exploring other

⁶⁴ Langmuir, I. *J. Am. Chem. Soc.* **1916**, 38, 11, 2221.

compounds with a similar metal-ligand bonds, such as potassium-imido nitride polytungstate,⁶⁵ we discovered the low growth rate was due to the slow oxidation of the tungsten-amine complex present in $(t\text{BuN})_2(\text{Me}_2\text{N})_2\text{W}$. The reaction between a tungsten-imido nitride and water generally takes an amount of time on the order of seconds to react in at atmospheric pressure. Figure 3.2 shows the growth rate with varied tungsten pulse (a) and relationship between thickness and number of cycles (b) under low oxidizing conditions when the 5s ‘stopvalve’ step is removed from the ALD recipe in table 3.1.

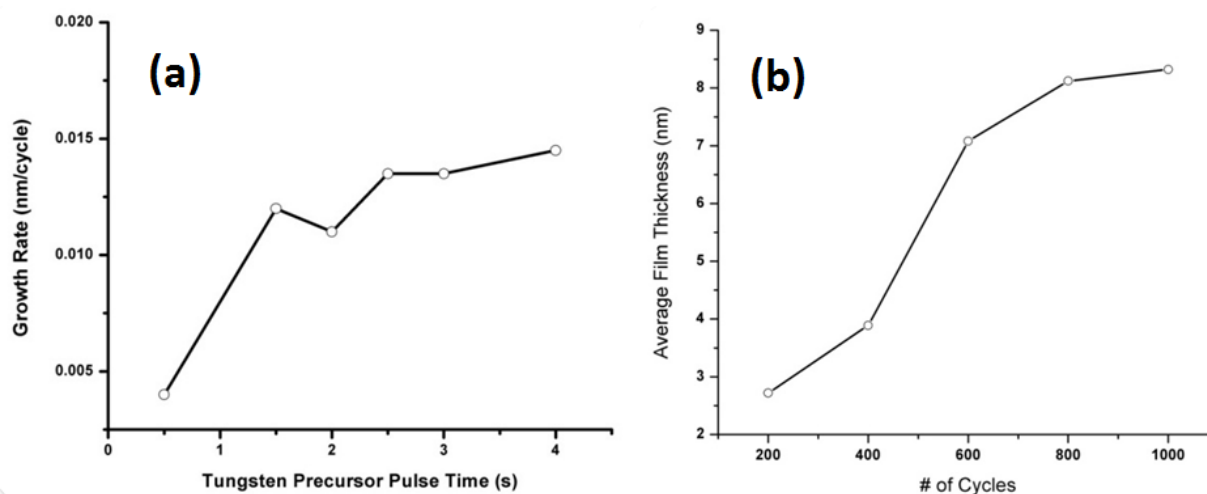


Figure 3.2 WO_3 growth characteristics with only a 0.05s water pulse and no additional exposure time. (a) shows that the growth is still self limiting for the tungsten precursor, while (b) shows an average growth rate of around 0.1 Å/cycle.

The growth however is very uniform and has good step coverage, as can be seen with a ~10 nm thick film grown on a silicon nanowire below.

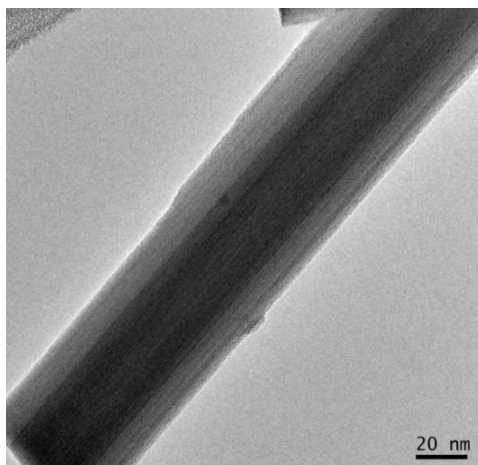


Figure 3.3 WO_3 grown on a SiNW after post-growth treatment. Low oxidation conditions were used in this growth, as described previously.

⁶⁵ Ostermann, D.; Jacobs, H. J. *Alloys Compds.* **1994**, 206, 15.

Figure 3.3 shows a thinner WO_3 film after 550°C annealing. Before annealing however it also has nanometer uniformity as shown below.

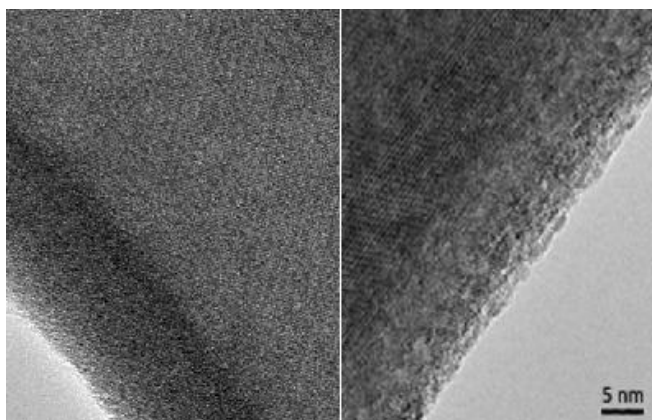


Figure 3.4 HRTEM of films grown on SiNWs before (left) and after (right) annealing.

As the film gets thicker its morphology gets rougher however (figure 3.5), still since it completely covers the substrate in the first few cycles as shown above it will work to protect our TiSi_2 NNs from the harsh oxidizing conditions of the water oxidation reaction.

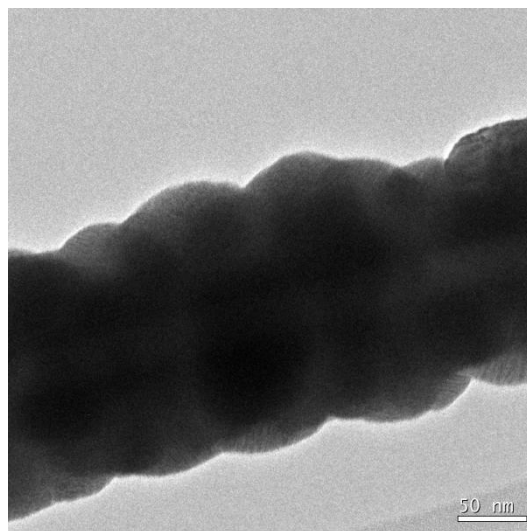


Figure 3.5 ~65 nm film growth on a SiNW before annealing, the presence of a rougher morphology suggests that this growth follows an 'island' ALD growth model where specific reactive sites initiate and continue the growth.

3.1.2 Post-Growth Treatment

As grown the film was slightly conductive and was a poor photocatalyst. This is because tungsten in the film was under-oxidized and the film had low crystallinity, in addition to being in a triclinic phase as opposed to a photocatalytic monoclinic phase. Therefore, after the synthesis,

the WO_3 film was placed in a tube furnace, which was then purged by an O_2 flow of 100 sccm for 10 min before the sample was heated up to a temperature varying from 350 °C to 550 °C. The heating rate was 4 °C/min. The annealing process lasted 1 h. The temperature was then brought down to room temperature at a rate of 4 °C/min. During the entire process, O_2 flow was constant.

Structural characterizations were carried out using a Scanning Electron Microscope (SEM, JSM-6340F), a Transmission Electron Microscope (TEM, JEM-2010F) and an X-ray Diffractometer (XRD, Bruker) to collect morphological and structural information. Elemental analysis and binding energy characterizations were performed on an X-ray Photoelectron Spectrometer (XPS, Kratos AXIS Ultra Imaging Spectrometer) and an Energy Dispersive Spectrometer (Oxford Instruments). The thickness of WO_3 was measured by ellipsometry (J.A. Wollam Co., Inc. Spectroscopic Ellipsometer) and cross-sectional TEM. To prepare the cross-section TEM sample, we employed a focused ion beam microscope (FIB, JOEL 4500 Multibeam system). A carbon film ($\sim 2 \mu\text{m}$ thick) was pre-deposited onto the WO_3 film to reduce ion beam damage. The sample was then milled into thin slices ($\sim 15 \mu\text{m} \times 5 \mu\text{m}$ span and $1.5 \mu\text{m}$ thick) with a 30-kV gallium (Ga) ion beam. A slice was cut off the substrate and transferred to a Cu support with a nano-manipulator (Kleindiek Nanotechnik MM3A). After it was glued to the Cu support, the slice was further thinned to be e-beam transparent ($< 100 \text{ nm}$ thick). A final polish with low-energy ion beam (5 kV) was applied to remove or minimize ion beam damage introduced in the previous steps. The absorbance of WO_3 was measured by a UV-Vis spectrometer (Ocean Optics USB 4000). Reflectance was also measured using an integrating sphere (Sphere Optics) coupled with a spectrometer (Ocean Optics USB 4000). For this, we grew WO_3 on quartz to eliminate potential influence of the ITO coating.

As-grown WO_3 is characterized by a high density of defects. This is evident in the cross-sectional TEM image (figure 3.6a) and the selective area electron diffraction (SAED) pattern (figure 3.6b).

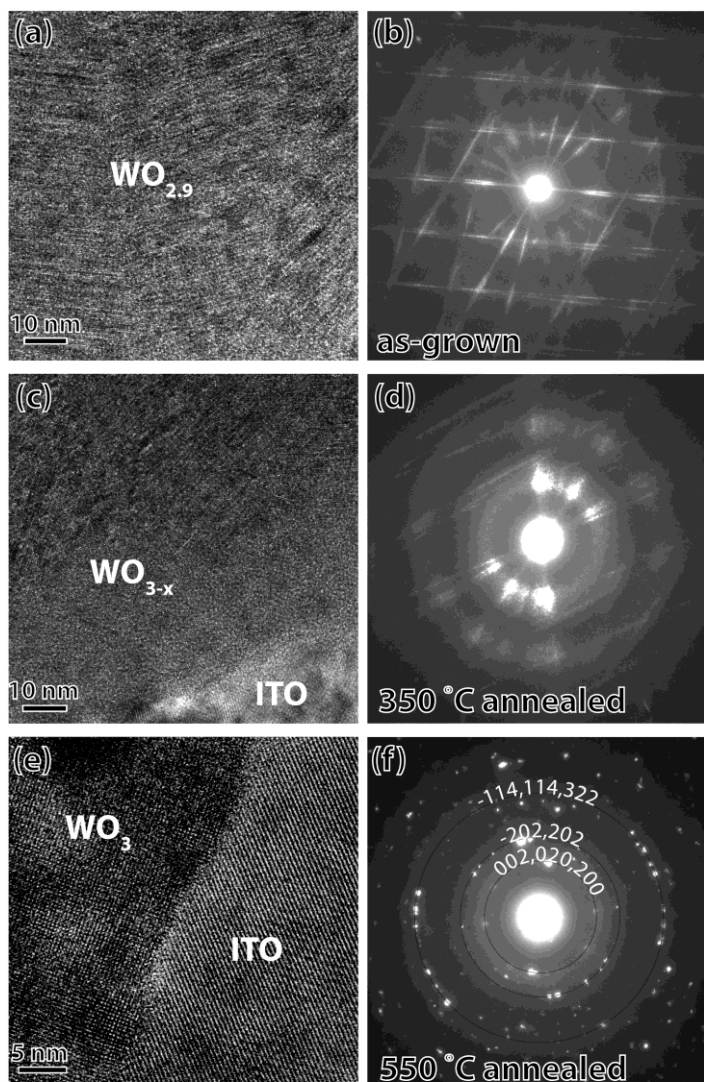


Figure 3.6 Microstructures of WO_3 studied by TEM and SAED.

(a) & (b) As-grown WO_3 is identified as $WO_{2.9}$. Here we can see a high defect density, manifested as stripes in the high-resolution TEM picture.

(c) & (d) After annealing at 350 °C, the defective $WO_{2.9}$ is transformed into amorphous WO_{3-x} as indicated in both the high-resolution image and the diffraction pattern.

(e) & (f) Polycrystalline WO_3 is obtained after 550 °C annealing.

The existence of defects is likely caused by the insufficient oxidation of the W precursor under the growth conditions. The result is in line with previous knowledge of WO_3 as oxygen vacancies and structural defects are common in WO_3 .⁶⁶ These defects can be reduced by annealing in O_2 as can be observed in the TEM images in figure 3.6a.

A phase transition from triclinic to monoclinic is observed in the TEM images, the XRD patterns, and the XPS data (figure 3.7).

⁶⁶ Niklasson, G. A.; Granqvist, C. G. *J. Mater. Chem.* **2007**, *17*, 127.

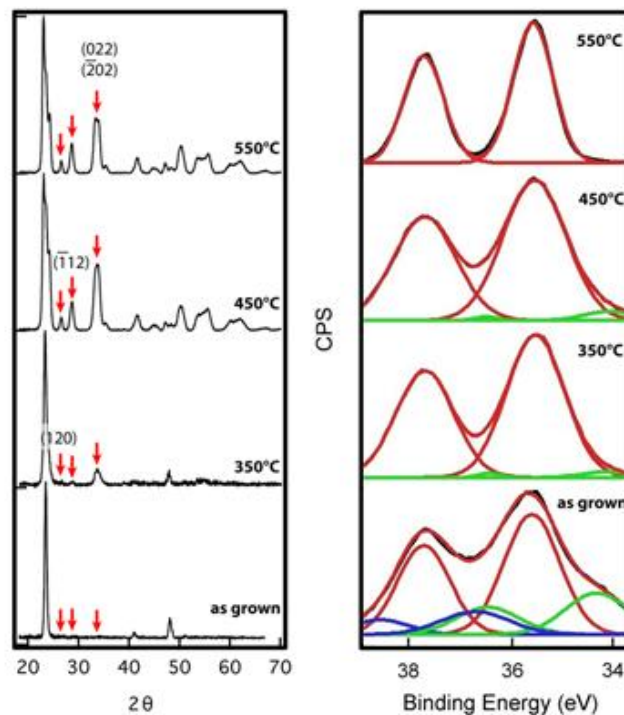


Figure 3.7 XRD (left) and XPS (right) spectra for the WO_3 films.

We found that 550°C was sufficient to achieve monoclinic WO_3 , which also gave the best results in PEC measurements. The XRD data also allowed us to identify the as-grown material as triclinic $\text{WO}_{2.9}$ with low crystallinity (JCPDS 18–1417).⁶⁷ Upon annealing, it is transformed into stoichiometric, monoclinic WO_3 (JCPDS 43-1035).⁶⁸ The (022) and ($\bar{2}02$) peaks ($2\theta = 33.3^\circ$ and 33.6° , respectively) of the XRD patterns are enhanced as a result of this transformation. In addition, the $2\theta = 48.1^\circ$ peak that may be assigned to $\text{WO}_{2.9}$ (220) disappears. As shown in figure 3.6, the crystallization appears to undergo a transformation from crystalline $\text{WO}_{2.9}$ (as-grown, Figure 3.6a and b) to a state where amorphous and crystalline WO_{3-x} coexist (350 °C annealed, Figure 3.6c and d), and finally to a state of polycrystalline WO_3 (550 °C annealed, Figure 3.6e and f).

Consistent with the removal of defects caused by oxygen vacancies and the structural data, the oxygen to tungsten ratio in the films was measured by XPS to be 2.60 before annealing. It was increased to 3.06 afterwards, suggesting further incorporation of oxygen during annealing. We also note that there are discrepancies in the exact values of the oxygen to tungsten ratio, 2.6 by XPS compared to 2.9 by XRD before 550 °C annealing, and 3.06 by XPS versus 3 by XRD after the annealing. This originates from a sampling difference between the two different characterization techniques. While XPS examines only the few atomic layers on the surface, XRD samples the entire material. The relatively high oxygen level on the surface of WO_3 after annealing suggests that additional oxygen is incorporated through diffusion from the surface. The binding energies of the W4f electrons also provide evidence of oxygen incorporation; prior

⁶⁷ Molloy, K. C.; Williams, P. A. *Appl. Organomet. Chem.* **2008**, 22, 676.

⁶⁸ Sallard, S.; Brezesinski, T.; Smarsly, B. M. *J. Phys. Chem. C* **2007**, 111, 7200.

to the annealing, we observed shoulders in the lower binding energy region ($4f_{7/2} = 36.7$ eV & $4f_{7/2} = 34.3$ eV) next to the main peaks ($4f_{7/2} = 37.7$ eV & $4f_{7/2} = 35.6$ eV) as shown in figure 3.7. These shoulders disappeared in the annealed samples.

Optically we found that the films changed color as a result of the annealing from blue to yellow. Blue tungsten oxide is usually a hydrated form of WO_3 ; while yellow WO_3 has its color due to band gap absorption of blue light (~ 450 nm), the color of the as-grown blue $\text{WO}_{2.9}$ can be attributed to the crystal field stabilization energy (CFSE) of the tungsten ion in a lower oxidation state. As the oxidation state of a tungsten ion decreases due to oxygen vacancies, the crystal field generated by surrounding oxygen ions gets weaker. This causes d -orbital splitting to lessen, forming energetic states that weakly absorb long wavelengths. This can be seen by a small increase in below band-gap absorption present in the absorption spectra below for as grown and 350°C annealed samples (figure 3.8a), causing the reflection of a small amount of blue light which gives it its bluish color.

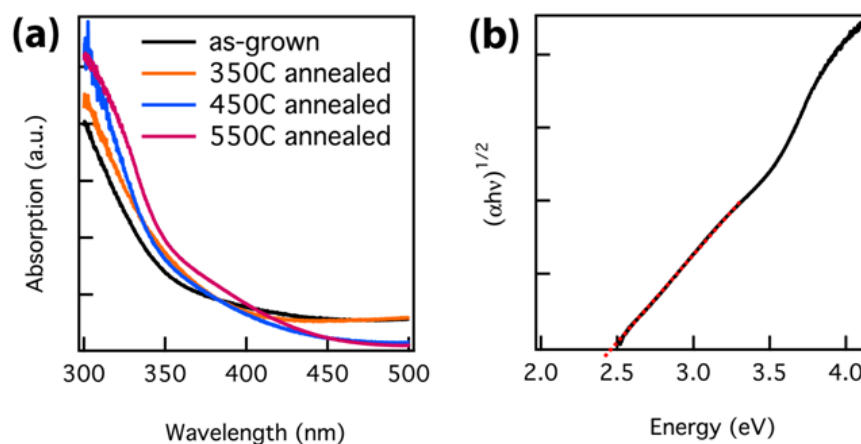


Figure 3.7 (a) absorption spectra for WO_3 films with different annealing conditions and (b) Tauc plot for 550°C annealed films.

Figure 3.8b uses the Tauc equation for an indirect band gap, described in section 2.1.2, to calculate the band gap of the annealed material at 2.5 eV.

As mentioned previously, the as-grown tungsten oxide had a blue color due to the CFSE of its low oxidation state tungsten ion. The film was also slightly conductive; when it was immersed in a solution with positive ions and a negative bias was applied, we observed insertion of the positive ions into the $\text{WO}_{2.9}$ crystal lattice. As a result, the local oxidation state in unit cells of $\text{WO}_{2.9}$ was increased due to the presence of an additional positive ion. This strengthened the crystal field in the lattice, causing a larger degree of d -orbital splitting than before and preventing lower energy photons from being absorbed. This caused the film to turn orange, since its d -orbital splitting was no longer small enough to absorb orange or yellow light. The conductivity of our $\text{WO}_{2.9}$ films also afforded us fast switching between blue and yellow.

3.2 Application of WO₃ Synthesis to Ti_{0.7}W_{0.3}O₂ Thin Films

Concurrent to developing the WO₃ thin film growth, we developed a Ti_{0.7}W_{0.3}O₂ ALD growth by incorporating (tBuN)₂(Me₂N)₂W into a typical TiO₂ film growth. This was in an attempt to reduce the band gap of the TiO₂ films used in our heteronanostructures. We found that the band gap of the film was indeed greatly reduced while many of the characteristics of a TiO₂ growth were retained.⁶⁹

3.2.1 Growth and Characterization of Ti_{0.7}W_{0.3}O₂ Thin Films

TiO₂ ALD using Ti(OⁱPr)₄ and water is well documented and known to be an ALD process.⁷⁰ Therefore, incorporating tungsten into the growth by use of (tBuN)₂(Me₂N)₂W involved only adding the precursor to the ALD sequence without the need to introduce any additional oxidants. The substrate was heated to 325°C, while Ti(OⁱPr)₄, (tBuN)₂(Me₂N)₂W and water were maintained at 75°C, 72°C, and 25°C (room temperature), respectively, throughout the growth. N₂ flowing at 10 sccm was used as a purging gas. The following ALD recipe was then used each cycle:

Operation	Ti Pulse	Purge	H ₂ O Pulse	Purge	W Pulse	Purge	H ₂ O Pulse	Purge
Time (s)	0.1s	5s	0.01s	10s	3s	5s	0.01s	10s

Table 3.2 One ALD cycle for Ti_{0.7}W_{0.3}O₂ thin film growth with a growth rate of 0.30 Å/cycle. Metal precursors are abbreviated.

We also tried other ratios of Ti(OⁱPr)₄ and (tBuN)₂(Me₂N)₂W to control the amount of tungsten in the film, however the recipe in table 3.2 resulted in the lowest band gap and best PEC performance. Since this is in essence a modified TiO₂ growth and it still falls in the ALD regime, it formed a conformal coating around TiSi₂ NNs. EDX and XRD were used to confirm that tungsten is incorporated into the film, and it was found that the film retained the anatase TiO₂ crystal structure.

⁶⁹ Lin, Y.; Zhou, S.; Liu, X.; Sheehan, S.; Wang, D. *J. Am. Chem. Soc.* **2009**, 131, 2772.

⁷⁰ Rahtu, A.; Ritala, M. *Chem. Vap. Deposition* **2002**, 8, 21.

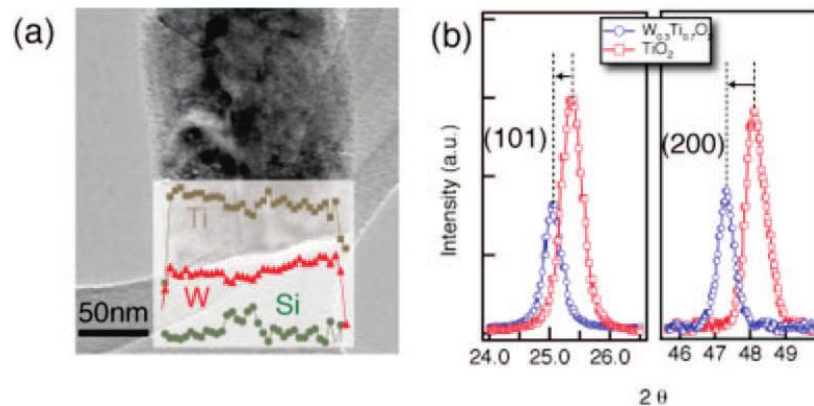


Figure 3.8 (a) TEM micrograph with overlaid elemental analysis of $\text{Ti}_{0.7}\text{W}_{0.3}\text{O}_2$ grown on TiSi_2 NNs showing that tungsten successfully incorporated into the film. (b) XRD spectra of anatase (101) and (200) peaks for TiO_2 and $\text{Ti}_{0.7}\text{W}_{0.3}\text{O}_2$. We can see a change in lattice constant representative of a distortion in the anatase crystal. Reproduced from [69].

The addition of tungsten caused a lattice distortion, evident in the XRD spectra in figure 3.8b, and reduced the band gap of the film to ~ 2.0 eV. However it also reduced the stability of the film, as neutral and basic solutions degraded its PEC performance by etching out the tungsten in the film. Below we can see absorption spectra and a Tauc equation plot showing the reduction in band gap from 3.2 eV to 2.0 eV.

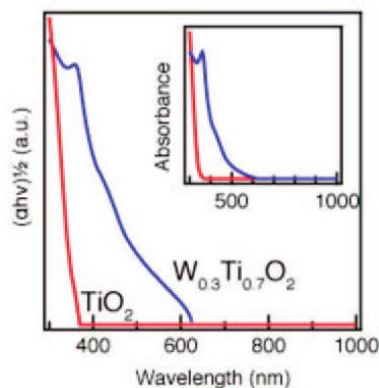


Figure 3.9 Band gap calculations for TiO_2 and $\text{Ti}_{0.7}\text{W}_{0.3}\text{O}_2$ showing a large increase in the overall absorption and decrease in the band gap of the film. Reproduced from [69].

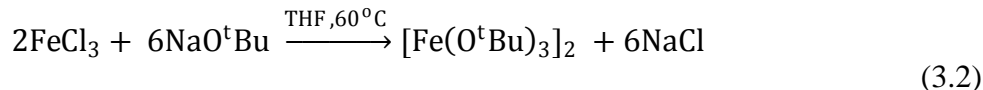
Incorporation of the $\text{Ti}_{0.7}\text{W}_{0.3}\text{O}_2$ films as a proof of concept for visible light water splitting was also successful (section 4.1.2). This showed that photons absorbed by this new material could be utilized for PEC applications.

3.3 Synthesis of Fe₂O₃ Thin Film

Unlike the ALD growths of WO₃ and Ti_{0.7}W_{0.3}O₂, synthesis of a Fe₂O₃ thin film by ALD has been demonstrated before.⁷¹ Previously, it has been used for magnetic applications and nanostructure synthesis.⁷² The novelty of our approach is its use as a thin film photocatalyst when interfaced with TiSi₂ NNs, which is described in the next chapter. Therefore, this section includes a brief summary of our experimental findings and structural characterizations.⁷³

3.3.1 Synthesis of [Fe(O^tBu)₃]₂ Precursor and Fe₂O₃ Thin Film Growth

In order to synthesize [Fe(O^tBu)₃]₂, 6.3g of NaO^tBu (97%, Aldrich) was mixed with 3.2g FeCl₃ (anhydrous, Aldrich) in 240 mL anhydrous tetrahydrofuran under argon. The reaction was heated to 60°C for 5 hours using a water bath, and then the solvent was removed by distillation at 80°C.



Following this, the dark green solid [Fe(O^tBu)₃]₂ was transferred into a precursor bubbler along with the NaCl byproduct.

The [Fe(O^tBu)₃]₂ was held at 140°C while water was 25°C (room temperature) throughout the deposition process. The substrate was heated to 180°C with N₂ flowing at 10 sccm. The growth took place in the same ALD system as the previous two growths; and in a similar manner one ALD cycle for Fe₂O₃ growth is defined as follows,

Operation	[Fe(O ^t Bu) ₃] ₂ Pulse	'Stopvalve'	N ₂ Purge	H ₂ O Pulse	'Stopvalve'	N ₂ Purge
Time (s)	5s	15s	10s	0.05s	15s	10s

Table 3.3 One ALD cycle for Fe₂O₃ thin film growth.

This recipe resulted in a growth rate of ~0.62 Å/cycle, after which samples were annealed to improve crystallinity under O₂ for 15 minutes at 500°C. Figure 3.10 shows a linear relationship between thickness and number of cycles, along with an SEM image of the film showing its uniformity to demonstrate that the growth falls within the ALD regime.

⁷¹ Mathur, S.; Veith, M.; Sivakov, V.; Shen, H.; Huch, V.; Hartmann, U.; Gao, H. B. *Chem Vap. Deposition* **2002**, 8, 277.

⁷² Bachmann, J.; Jing, J.; Knez, M.; Barth, S.; Shen, H.; Mathur, S.; Gosele, U.; Nielsch, K. *J. Am. Chem. Soc.* **2007**, 129, 9554.

⁷³ Lin, Y.; Zhou, S.; Sheehan, S.; Wang, D. *J. Am. Chem. Soc.* **2011**, 133, 2398.

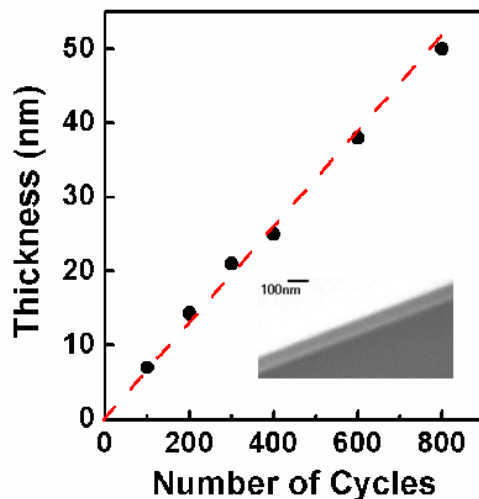


Figure 3.10 Thickness of grown film versus number of cycles, with SEM image of a 100 nm film on n-Si(100) (inset). Graph reproduced from [73].

Structural characterization of the film included XRD and XPS to identify the film as α - Fe_2O_3 . While iron was in the oxidation states needed to form hematite, as-grown the film had very poor crystallinity. Below is an XRD spectra of the film before and after annealing, showing the improvement in crystallinity caused by the 15 minute, 500°C annealing.

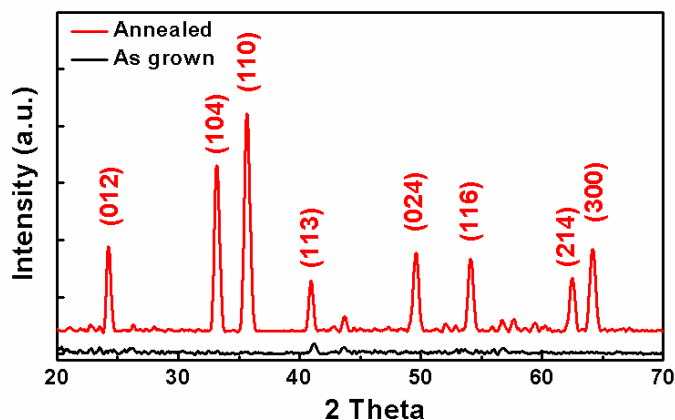


Figure 3.11 XRD spectra of Fe_2O_3 before and after annealing. Reproduced from [73].

And below is the XPS spectrum of the iron 2p region before annealing, no change was observed after annealing. This spectrum also agrees with other literature reports on hematite, one of which is shown side by side for comparison.⁷⁴

⁷⁴ A. A. Tahir, K. G. Wijayantha, S. Saremi-Yarahmadi, M. Mazhar, V. McKee, *Chem. Mater.*, **2009**, 21, 3763.

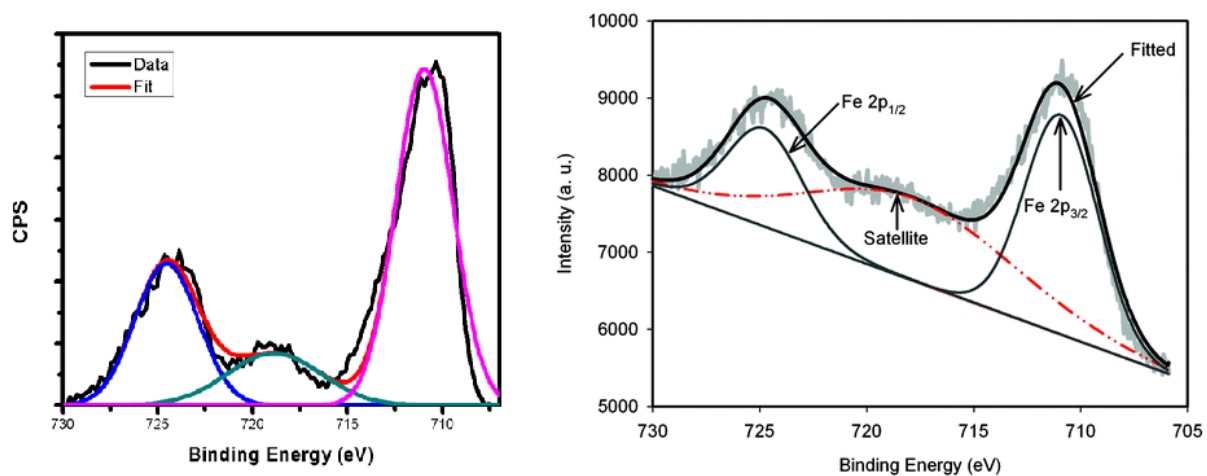


Figure 3.12 XPS spectra of Fe_2O_3 before annealing, no change was seen after annealing. Left graph is the data and peak fitting from this study; right graph reproduced from [74].

After determining that our film was highly crystalline and stoichiometric Fe_2O_3 , band gap calculations were performed from absorption spectroscopy measurements.

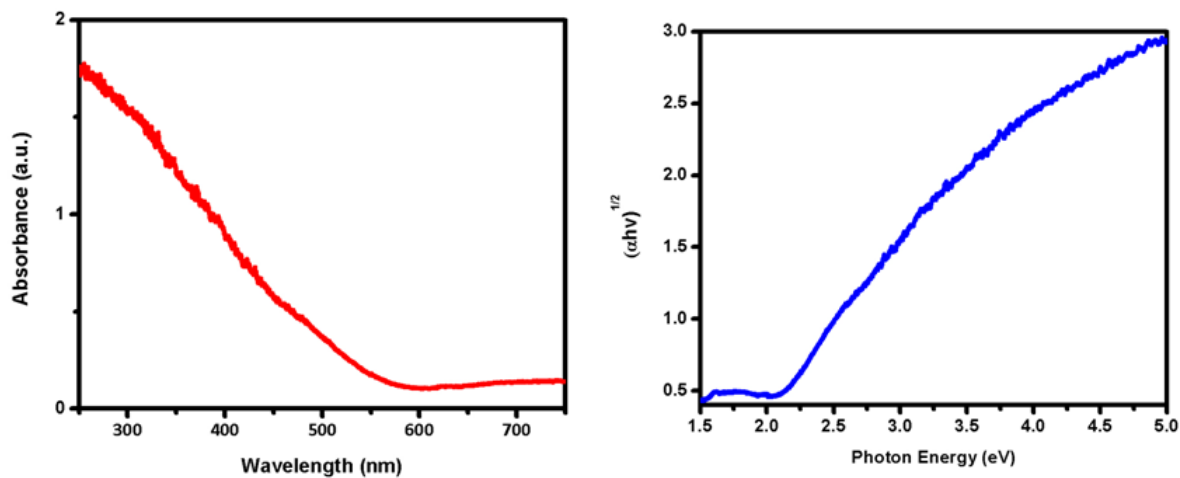


Figure 3.13 Absorption spectra and Tauc plot for Fe_2O_3 . The band gap of the thin film is ~ 2.1 eV.

This confirmed that the band gap of our material is in the visible light region and suitable for water splitting.

Chapter 4

Photocatalysis with Heterostructured Photoanodes

4.1 TiSi₂ Nanonet Heterostructures for Water Splitting

A major dilemma in solar cell design is the compromise that is made between absorption and carrier recombination. In most solar cell materials, the penetration depth of visible and UV light is much longer than the diffusion length of charges in the material. Therefore a thick material will absorb light well, but as a consequence charges will have to travel farther to reach an electrode and thus have a higher chance of recombination. A thin material requires that charges be transported a shorter distance and therefore have a lower chance of recombination, but it will not be able to absorb as much light.

One way of overcoming this roadblock in solar cell design is by decoupling the paths of light absorption and charge separation in a material. This can be achieved by controlling its morphology, in this case by depositing a photoanode material on a conductive nanonet structure. This serves to orthogonalize the path of light absorption to the path of charge separation so that light is absorbed in a direction perpendicular to the direction charges must travel. By doing this, we can make a structure that absorbs light as well as a thick material and has a rate of recombination similar to that of a thin material, therefore increasing solar cell efficiency. In addition to this, a photoactive material thinner than its depletion width has a built-in field throughout the material which makes charge separation and transfer energetically favorable.

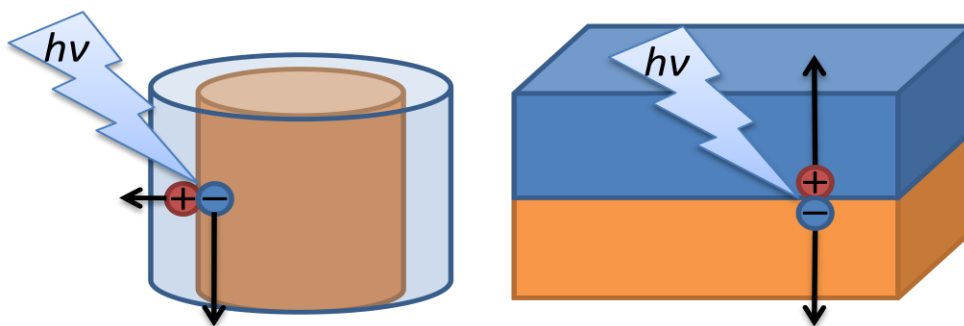


Figure 4.1 Schematic of the concept, the figure on the right represents part of a planar solar cell while the figure on the left represents part of a nanostructured one, such as the nanonet heterostructures covered in this chapter. Arrows represent the path of charge separation. We can clearly see that charges need not travel as far in the nanostructure.

This section uses the PEC methods and terminology outlined in chapters 1 and 2 to characterize these heteronanostructures made for water splitting. Previously, the synthesis, structural, and spectroscopic characterization of WO_3 , $\text{Ti}_{0.7}\text{W}_{0.3}\text{O}_2$, and Fe_2O_3 were covered, and TiO_2 is widely reported in literature. Each of these films was synthesized on conductive TiSi_2 nanonets and used as a photoanode for water splitting, and in all of these tests the presence of O_2 bubbles evolving at the anode and H_2 at the cathode of the PEC cell was easily visible. Here, their efficiencies and PEC properties are compared with each other and with planar films to show a clear improvement and confirm that the heteronanostructure architecture greatly improves the overall efficiency of water splitting photoanodes.

4.1.1 $\text{TiO}_2/\text{TiSi}_2$

We conducted current-voltage measurements with a CHI 600C Potentiostat in a three electrode configuration, using platinum mesh as the counter electrode and Ag/AgCl in 1M KCl as the reference electrode. The difference between Ag/AgCl and the RHE is 0.236 V at room temperature. The $\text{TiO}_2/\text{TiSi}_2$ working electrode was grown on titanium foil, a contact was made using copper wire and conductive silver epoxy (SPI), and the substrate was covered with a non-conductive hysol epoxy (Loctite) except for the front side where the heteronanostructures were present. The electrodes were immersed in a 0.05M KOH solution, and the potential was linearly swept from -1 V to 0 V vs. Ag/AgCl at a scan rate of 50 mV/s. Light sources used included a 150 W Xenon lamp, a 450 W Xenon lamp coupled with a monochromator (Jobin Yvon Fluorolog3, bandpass 5 nm) and a 150 W solar simulator (Oriel 96000, equipped with AM 1.5 filter). Two types of filters were employed, both of which had a cutoff frequency of 400 nm. One type was utilized to filter photons with wavelength longer than 400 nm for measurements using UV light, and the other was used to filter wavelengths shorter than 400 nm for measurements in visible light.

While the 3-electrode system described above is sufficient to compare our results to others in literature, a 2-electrode system must be used to accurately measure efficiency as covered in section 1.3. In the following IPCE and efficiency measurements, a two electrode system was used, wherein the heterostructure served as the anode and Pt mesh was used as the cathode. They were connected to a Keithly 2400 sourcemeter which provided a 0.5 V bias with

the same electrolyte and illumination conditions as in the three electrode measurements. IPCE and overall efficiency were then calculated using equations 2.4 and 1.15, respectively.

In order to optimize the system, different thicknesses of TiO_2 were grown on planar substrates and on nanonets to determine what thickness would yield the best photocurrent. Figure 4.2 details the results of this study; it also demonstrates that the heteronanostructure approach gives higher overall photocurrents than planar films, as expected.

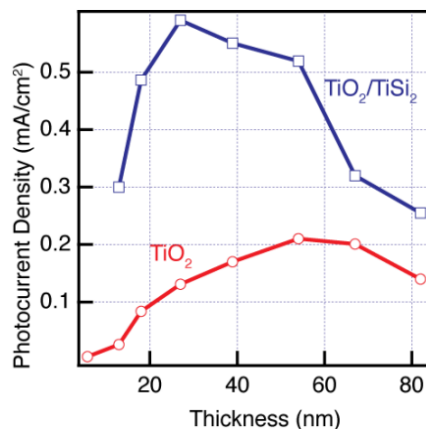


Figure 4.2 Photocurrent dependence on TiO_2 thickness under 150 W Xe lamp irradiation At 0 V vs, Ag/AgCl. Reproduced from [75].

27 nm was determined to be the optimum thickness for films grown on nanonets, while 55 nm was best for planar TiO_2 . Optimum thickness for the $\text{TiO}_2/\text{TiSi}_2$ heterostructure is less than that of the planar film since the planar film needs a required thickness to absorb enough light for efficient charge collection, while the heterostructure absorbs enough light due to its morphological advantage. Therefore it is more dependent on the necessary depletion width for charge separation in the material, which is smaller.

Due to the wide band gap of TiO_2 at 3.2 eV, no photocurrent was seen under visible light (using the aforementioned wavelength filter). Figure 4.3a shows a significant V_{oc} (-0.8 V vs Ag/AgCl) indicating efficient charge separation and high anodic I_{sc} (-0.6 mA/cm^2 at 0 V vs Ag/AgCl) under xenon light which shows that the structure is absorbing light efficiently. Low dark current was seen, signifying that band bending was formed between TiO_2 and the electrolyte which prevented charge transfer in the absence of the chemical potential difference afforded by light irradiation.

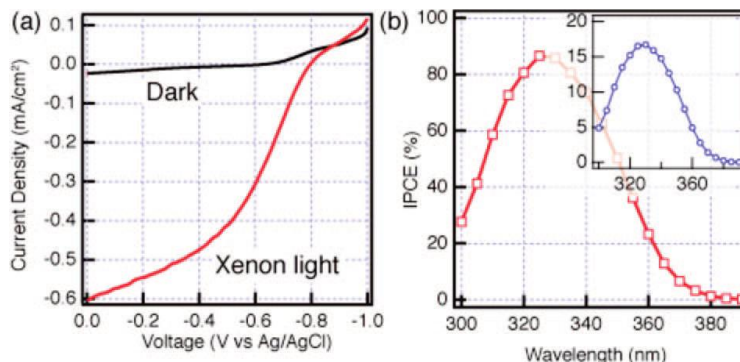


Figure 4.3 (a) *I-V* plot of the PEC cell in a 3-electrode configuration showing photocurrent. (b) IPCE and overall efficiency (inset) taken in a 2-electrode configuration. Reproduced from [75].

As expected, in figure 4.3b IPCE drops off at wavelengths >385 nm. Peak efficiency under monochromatic light for the device occurred at 330 nm and was 16.7%.⁷⁵

4.1.2 $\text{Ti}_{0.7}\text{W}_{0.3}\text{O}_2/\text{TiSi}_2$

Along with the $\text{TiO}_2/\text{TiSi}_2$, we studied $\text{Ti}_{0.7}\text{W}_{0.3}\text{O}_2/\text{TiSi}_2$ heteronanostructures. The same set-up as is in the previous section, including a similar film thickness, was used with the aforementioned AM 1.5 solar simulator as a light source. The electrolyte was also changed to 0.05 M HCl since $\text{Ti}_{0.7}\text{W}_{0.3}\text{O}_2$ corrodes in solutions with $\text{pH} > 4$. Figure 4.4 shows that the majority of photocurrent from the $\text{Ti}_{0.7}\text{W}_{0.3}\text{O}_2/\text{TiSi}_2$ heteronanostructures was found to come from visible light, which we could expect due to its low band gap if 2.0 eV.

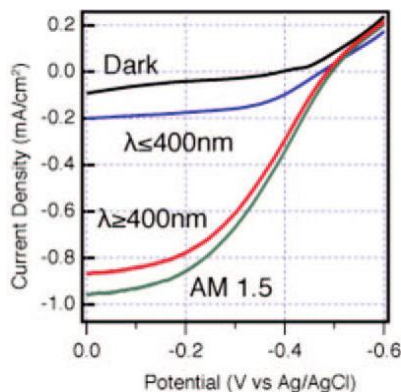


Figure 4.4 *I-V* plot of the PEC cell with a $\text{Ti}_{0.7}\text{W}_{0.3}\text{O}_2/\text{TiSi}_2$ nanonet heterostructure as the working electrode. Different illumination conditions were achieved using 400 nm cutoff filters and an AM 1.5 solar simulator. Reproduced from [75].

The efficiency of this structure under AM 1.5 irradiation was calculated to be 0.83%, which shows as a proof of concept that these heterostructures are efficient in converting sunlight to chemical energy.

⁷⁵ Lin, Y.; Zhou, S.; Liu, X.; Sheehan, S.; Wang, D. *J. Am. Chem. Soc.* **2009**, 131, 2772.

4.1.3 WO₃/TiSi₂

Since WO₃ has a weaker absorption than TiO₂ in addition to a shorter carrier diffusion length, interfacing it with TiSi₂ NNs caused an even greater increase in photocurrent than it did in TiO₂. Conditions for the PEC cell and 2/3-electrode measurements are similar to the previous two sections, except that a 0.1 M HCl solution was used due to the sensitivity of WO₃ films to corrosion by neutral and basic electrolytes. Prior to a measurement, the electrolyte solution would be bubbled with N₂ to eliminate any contribution to photocurrent from dissolved O₂, and the devices would be cleaned by UV-Ozone (Jelight Company Inc.) exposure for 3 minutes.

Figure 4.5 shows comparisons of WO₃ films grown on nanonets subjected to different annealing conditions showing that as the film crystallinity improves, photocurrent also improves. Also in figure 4.5, we can see an over 4-fold increase in photocurrent for films grown on a planar substrate versus films grown on nanonets. This further reinforces our hypothesis that heteronanostructures can be used to improve PEC cell efficiency by using films with thickness close to a material's charge diffusion length.

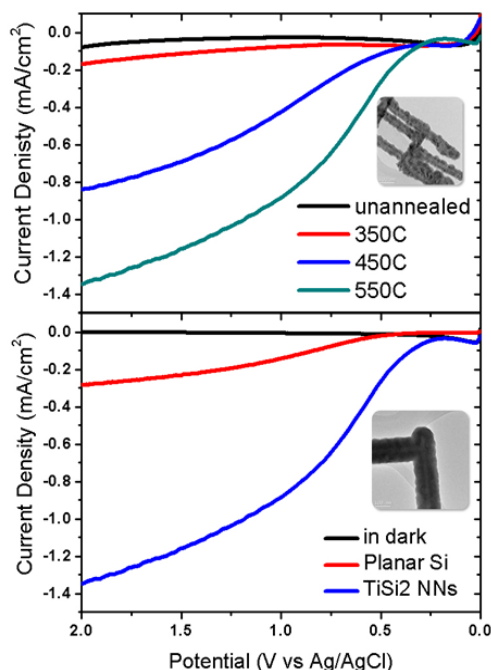


Figure 4.5 I-V plots for different WO₃ thin films grown on NNs and Si under 150 W Xe lamp irradiation in 1M HCl. Inset are TEM micrographs of 550 °C annealed WO₃/TiSi₂ nanonet heterostructures.

Other conditions, such as with the presence of a hole scavenger (methanol), were also explored and showed to increase photocurrent by mechanisms that have been previously studied.⁷⁶ Film thickness was optimized in a similar manner as was done with TiO₂/TiSi₂ heteronanostructures. Figure 4.6 below shows that ~43 nm is the optimum thickness for films grown on nanonets while planar films reached peak photocurrent at 120 nm for similar reasons as was discussed in 4.1.1.

⁷⁶ Santato, C.; Ulmann, M.; Augustynski, J. *Adv. Mater.* **2001**, 13, 511.

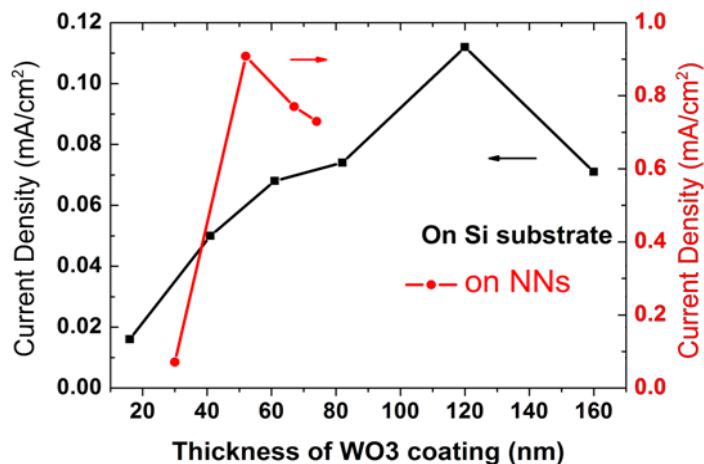


Figure 4.6 Photocurrent dependence on WO₃ thickness at 1.23 V vs. Ag/AgCl under 150 W Xe lamp irradiation.

IPCE of the film also shows that its efficiency converted visible light with its 2.5 eV band gap. A bias of 1.23 V vs RHE was used. The absorption and IPCE are similar with deviations around 350 nm which may be caused by an artifact the absorption measurements.

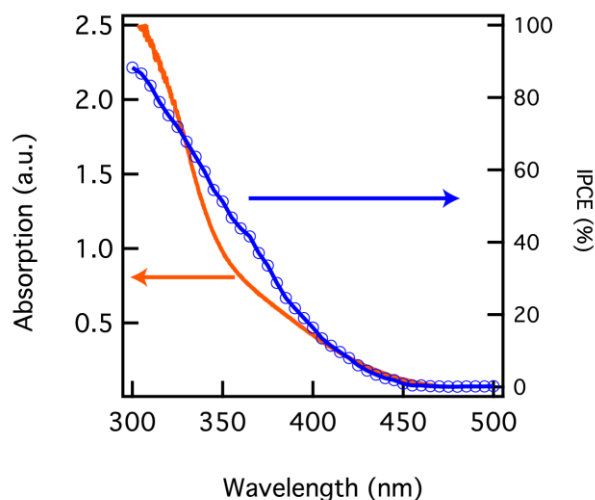


Figure 4.7 IPCE measured for WO₃/TiSi₂ NN heterostructures under monochromatic light with a 1.23 V vs RHE applied bias.

Figure 4.7 also highlights the poor absorption WO₃ has near its band edge, one of the major hurdles in water splitting with a WO₃ photocatalyst. Typically only thicker materials can compensate for this absorption loss near the band edge, though new materials such as these heteronanostructures are a promising new route toward overcoming this challenge.

4.1.4 Fe₂O₃/TiSi₂

The final water splitting material studied as a photocatalyst on a nanonet scaffold was hematite.⁷⁷ This study used a 25 nm hematite film on TiSi₂ NNs as a photoanode, and similar to the previous three sections took advantage of the heteronanostructure architecture by incorporating a film with thickness close to that of the diffusion length of charges to prevent excessive recombination. Experimental details are similar to the previous section, except were performed in a CHI 608C potentiostat, with Hg/HgO in 1M NaOH as a reference electrode. The electrolyte was a 1 M NaOH solution, with current flowing into the photoanode defined as positive. IPCE and APCE measurements were taken in 3-electrode configuration with a 1.53 vs RHE bias.

The highest IPCE measured for this heteronanostructure was 46% at 400 nm, which at the time was the highest attainable by undoped hematite without the presence of a co-catalyst.

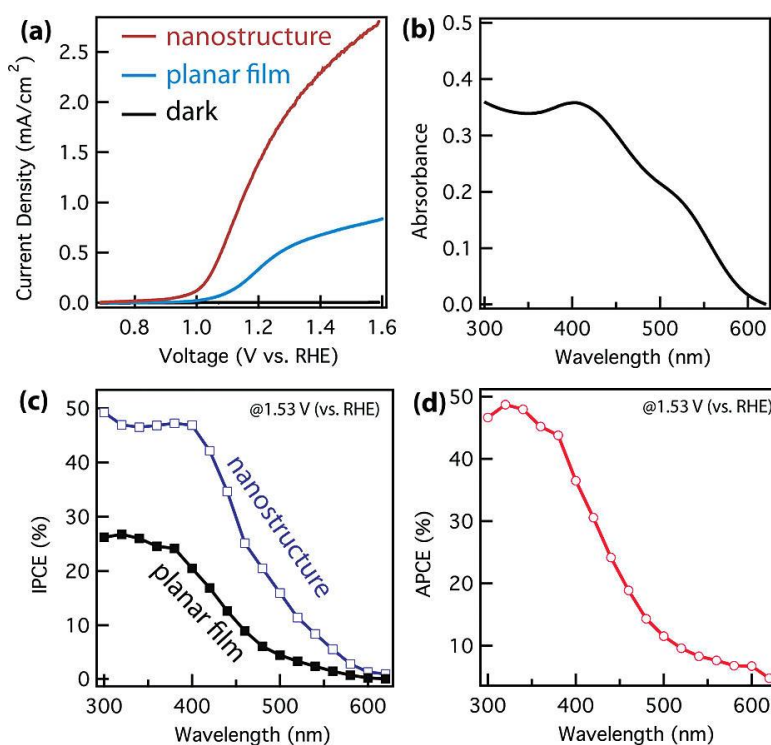


Figure 4.8 PEC properties of Fe₂O₃ thin films and heteronanostructures.

(a) I-V plot of Fe₂O₃ photoanodes grown on FTO and TiSi₂ NNs showing a clear increase in device performance. (b) Absorption spectrum for Fe₂O₃ used in APCE calculations. (c) IPCE comparison showing improved efficiency by utilizing nanonet architecture. (d) APCE of the film grown on planar FTO. Reproduced from [77].

Similar IPCE and the nanostructure and APCE of the planar film, shown in figure 4.8, demonstrate that the major hindrance in our system stems primarily from poor charge separation and transfer. It also shows that our heteronanostructure approach nearly maximized absorption without further hindrance of charge separation, such as would be the case with a thick film.

⁷⁷ Lin, Y.; Zhou, S.; Sheehan, S.; Wang, D. *J. Am. Chem. Soc.* **2011**, 133, 2398.

However, absorption near the band edge is particularly bad and must also be improved before efficient Fe_2O_3 solar cells can be realized.

4.2 WO_3/SiO_2

WO_3 is a well known catalyst for the photocatalytic degradation of 4-chlorophenol (4-CP, >99%, Aldrich).⁷⁸ In this study, we interfaced the WO_3 thin film with a cheap, high surface area, environmentally friendly catalyst that does not compete with absorption in a way the nanonets do. Silica gel (Sorbent, particle size: 20-45 μm , porosity: 60 \AA , surface area: 450-550 m^2/g) was used as the scaffold in this heterostructure. The ALD growth was also modified by increasing precursor exposure times by 3 seconds to allow precursor gases to fully coat the silica gel, and depositions took place using an aluminum boat fitted with a stainless steel porous disc (10 μm pore size, McMaster) to hold the silica particles. 60 nm thick films were grown on the silica gel particles; they were blue in color upon removal from the ALD, then turned yellow after annealing. 25 mg WO_3/SiO_2 was dispersed in 10 mL 4-CP aqueous solution (0.5 mM) through vigorous stirring for an hour in dark and then exposed to a Xenon lamp illumination (80 mW/cm^2). 4-CP concentration was periodically examined by absorbance measurements. Care was taken to exclude the potential influence of particle-induced scattering during the measurements. Control experiments with SiO_2 particles without WO_3 coating, and where no particles at all were used, were conducted for comparison.

The resulting heterostructures outperformed WO_3 nanoparticles as reported in literature.⁷⁹ Below is a graph showing the weighted concentration of 4-CP over time.

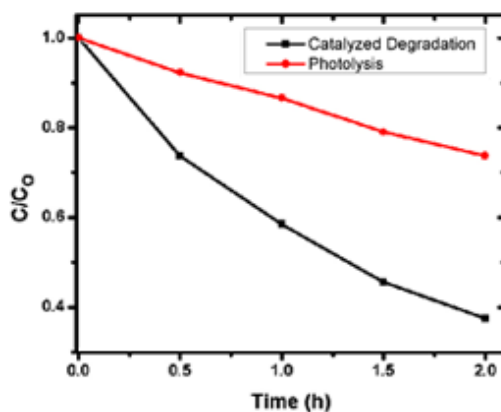


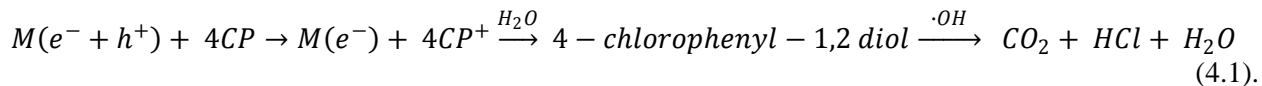
Figure 4.9 4-CP degradation with WO_3 catalyst under Xenon lamp illumination (black) compared to photolysis of 4-CP (red). The control sample containing uncoated silica gel gave the same results as the photolysis.

From this graph, we can see that 4-CP photolysis was shown to follow zero-order kinetics and catalyzed degradation exhibits pseudo-first order characteristics. Their rate constants were found to be 0.523 h^{-1} with the catalyst and 0.132 Mh^{-1} for photolysis.

⁷⁸ Waldner, G.; Brueger, A.; Gaikwad, N. S.; Newmann-Spallart, M. *Chemosphere*, **2007**, 67, 779.

⁷⁹ Lin, C.; Wu, C.; Onn, Z. *J. Hazard. Mater.*, **2008**, 154, 1033.

The mechanism of photodegradation uses WO_3 as a hole donor. As an example, one such reaction pathway for 4-CP degradation is represented in the following equation,



The remaining reaction pathways and a more detailed account of the degradation mechanism can be found in the review by Hiskia et al.⁸⁰ In the particle heterostructure, photoanode charge transfer principles still apply except there is no external circuit to send electrons to. Without an external circuit, there is also no way to apply a potential to the material, thus the only driving force sending holes into solution is band bending at the space charge region. Charge diffusion can also move charges closer to the surface, but it is extremely slow and inefficient when compared to the built-in field of the space charge region. This makes it favorable to synthesize films thinner than the depletion width of the material, a suitable task for an ALD growth. Preliminary tests of a $\text{TiO}_2/\text{SiO}_2$ heterostructure also were promising, suggesting that this architecture can be used with other catalysts and systems.

⁸⁰ Hiskia, A.; Mylonas, A.; Papaconstantinou, E. *Chem. Soc. Rev.*, **2001**, 30, 62.

Chapter 5

Investigation of Charge Carrier Dynamics with Time-Resolved Microwave Photoconductivity (TRMC)

5.1 Charge Transfer at the Interface

To explore the behavior of electrons and holes in the thin films we synthesized, a contactless method of measuring photoconduction dynamics was used to measure carrier lifetime in different environments. Using the TRMC method we can directly observe photogenerated charges in the film and at the semiconductor-liquid junction instead of having to infer charges' behavior by analyzing PEC and efficiency measurements. Using the experimental set-up outlined in section 2.1.4, films of Fe_2O_3 and WO_3 were measured with and without an electrolyte interface, in electrolytes having varied pH, and on a variety of substrates.

This first study compares Fe_2O_3 films in contact with different environments. The thin film was grown to 25 nm following the growth steps outlined in section 3.3.2; the 25 nm film was shown to have the best performance in a PEC cell and is smaller than the depletion width of Fe_2O_3 when interfaced with water. Therefore, when interfaced with an electrolyte, throughout this film the conduction and valence bands are bent making it favorable for holes to transfer into solution.

It is known that lifetime of photogenerated charges in bulk Fe_2O_3 can be as low as picoseconds, while the diffusion length can be as low as 4 nm.⁸¹ Since the TRMC system used in this study only measures down to the nanosecond range, attempting to measure a picoseconds signal is futile. Thin films, however, can exhibit longer lifetimes due to charge transfer out of the film or charge trapping at interfaces which are reached relatively rapidly. To this end, we tested 25 nm iron oxide thin films with four different interface conditions, grown on either a quartz or conductive fluorine-doped tin oxide (FTO) substrate and both with and without an electrolyte interface.

We were able to see changes in recombination dynamics in each of these four systems, and by relating them to each other we can determine what part of the system is responsible for

⁸¹ Kennedy, J. H.; Frese, K. W. *J. Electrochem. Soc.* **1978**, 125, 709.

recombination: the iron oxide film itself, the interface with quartz, the interface with the conductive substrate, or the interface with water. Recombination in this system may also be occurring in the conductive substrate or water, since charges at the surface may delocalize past the interface. Alternatively, the long lifetimes observed could be completely due to charge traps at each interface.

Another interesting observation in this study is the increase in measured lifetime of charges in ultrathin Fe_2O_3 by several orders of magnitude when a semiconductor-liquid junction is introduced. One explanation for this may lie in the surface chemistry of holes transferring from Fe_2O_3 to the electrolyte. This process contains multiple steps with different reaction rates that could be affected adversely by this system; for example we may be observing charge trapped at an intermediate state between the semiconductor and $\text{O}_2/\text{H}_2\text{O}$. Another explanation is that this effect is more reliant on semiconductor physics. Holes are being pushed toward the semiconductor-liquid junction by band bending but may not possess enough energy to transfer into water, in this case we would be creating a hole trap at the junction which would increase perceived lifetime.

Figure 5.1, below, shows a preliminary laser measurement of lifetime for a 25 nm iron oxide film on quartz both dry and wetted with pH 7 water. This measurement was done using a 388 nm, 400 fs laser pulse (see 2.1.4 for all experimental details).

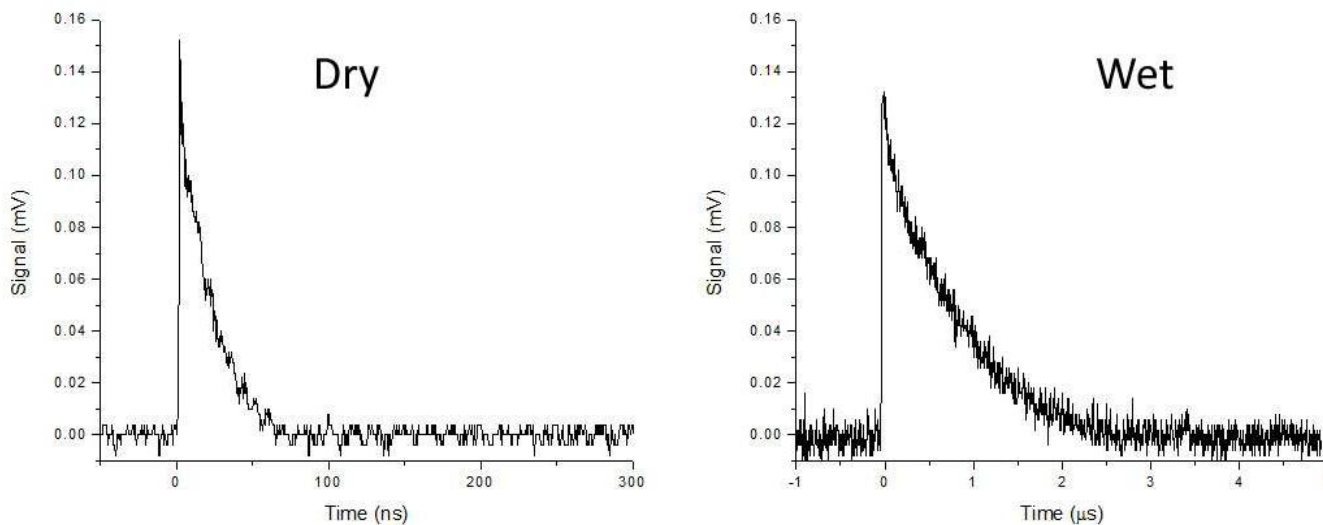


Figure 5.1 Comparison of carrier lifetimes for 25 nm Fe_2O_3 films grown on quartz, dry and wetted with deionized water.

These results were then reproduced using a xenon flashlamp. Since the FWHM of the xenon flashlamp pulse is 1.3 μs , in figure 5.2 the Fe_2O_3 film measured in dry conditions shows primarily the pulse characteristics of the flash lamp and not that of the film. This still illustrates the significant increase in photoconductance lifetime afforded by the semiconductor-liquid junction. Using equation 1.10 to fit the logarithm plot in figure 5.2, the measured lifetimes for wet and dry Fe_2O_3 on quartz are 2.0 μs and 0.5 μs , respectively.

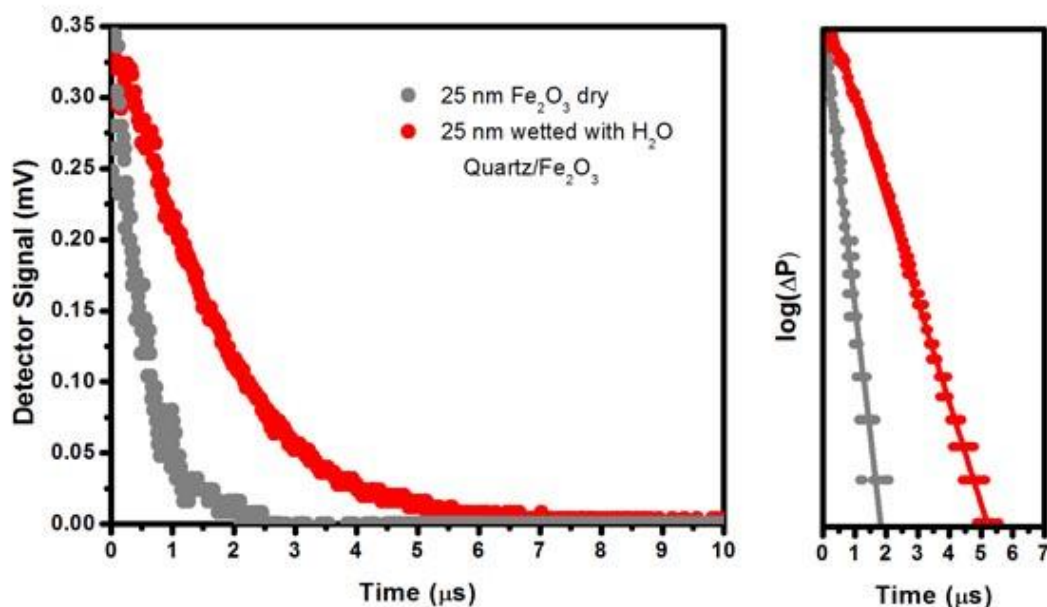


Figure 5.2 Photoconduction decay and logarithm plot for the Fe₂O₃/quartz system under xenon flashlamp illumination at 200 mJ. From the log plot we can directly see the increase in carrier lifetime due to the presence of water at the interface.

As controls and to continue this study, the film grown on quartz was compared to a Fe₂O₃ film grown on FTO. The film in dry conditions experienced a significant increase in carrier lifetime; however the carrier dynamics of the film in wet conditions was unchanged. This data suggests that we are seeing the slowest process occurring in the system when measuring photoconductance lifetime; and that the slowest recombination these measurements occurs when Fe₂O₃ is interfaced with water. This suggests charge trapping at the semiconductor-liquid junction, as mentioned previously. The nanosecond time scale on which recombination is occurring in dry conditions with Fe₂O₃ grown on quartz suggests that it is dominated by either recombination in Fe₂O₃ or very shallow traps at the Fe₂O₃/quartz interface. Similarly, recombination for the Fe₂O₃/FTO system may either be occurring in the conductive substrate, where recombination is likely without an external circuit to collect charge, or at shallow levels at the Fe₂O₃/FTO interface that are much deeper than that of the Fe₂O₃/quartz system. From this data, lifetime of charges that undergo recombination at the semiconductor-liquid junction are the longest; this may be because band bending is unfavorable for electrons to travel to the junction, therefore it takes more time for them to reach holes there to recombine. Below is an illustration representative of these three mechanisms along with corresponding time-domain decays.

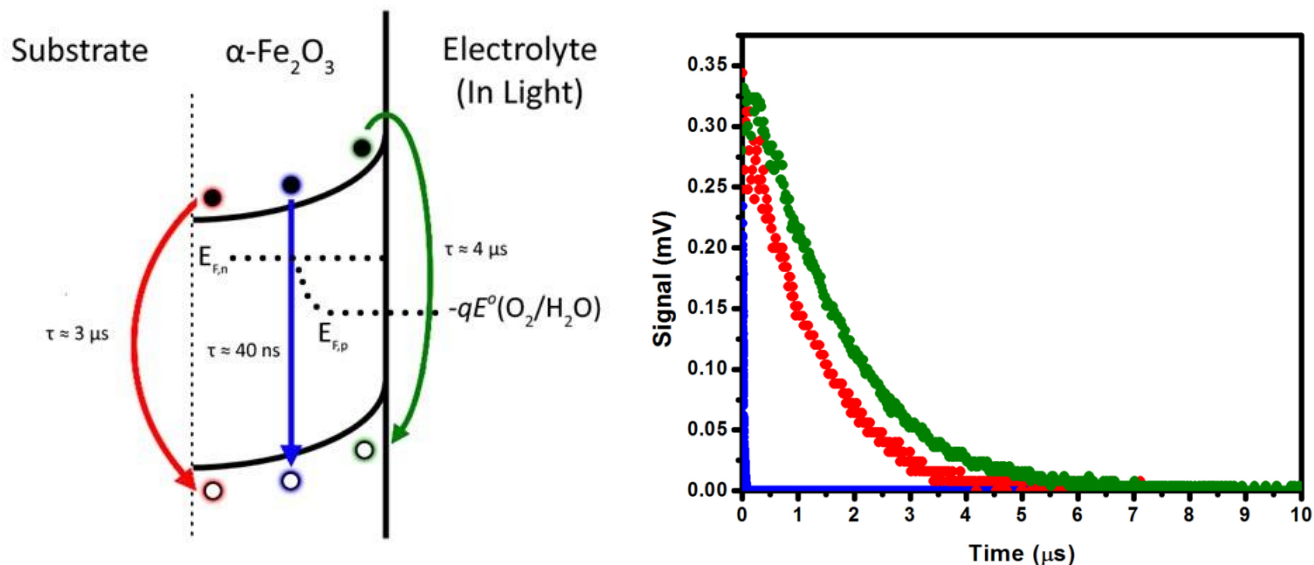


Figure 5.3 Band diagram with representations of recombination pathways and graph showing their color coded corresponding lifetimes. The diagram to the left is merely representative; further study is needed to fully understand how recombination occurs in these systems.

Note, however, that in the case of recombination under dry conditions for both films grown on quartz and FTO significant band bending does not occur, therefore there is little electric field to push charges toward a junction.

These results were reproducible also for the case of 40 nm thick WO_3 films (still lower in thickness than the film's depletion width), with which we have similar hypotheses for the fate of photogenerated charges. From these measurements and previous measurements with a Stevenson-Keyes contact measurement system,⁸² the decay of photoconductivity for WO_3 under dry conditions was found to take over 1 μs . This was later confirmed with the TRMC system. In water this increased to over 4 μs . Converting these decay measurements to logarithm plots and fitting with equation 1.10 gives a lifetime for dry WO_3 of 0.9 μs while wet WO_3 has a lifetime of 2.1 μs , a value close to that of Fe_2O_3 in water. This suggests a similar mechanism that is trapping holes in both semiconductors. A small increase in lifetime is also seen when WO_3 is interfaced with FTO as opposed to quartz, most likely caused by charge trapping at the interface or charge delocalization into FTO.

⁸² Stevenson, D. T.; Keyes, R. J. *J. Appl. Phys.* **1955**, 26, 190.

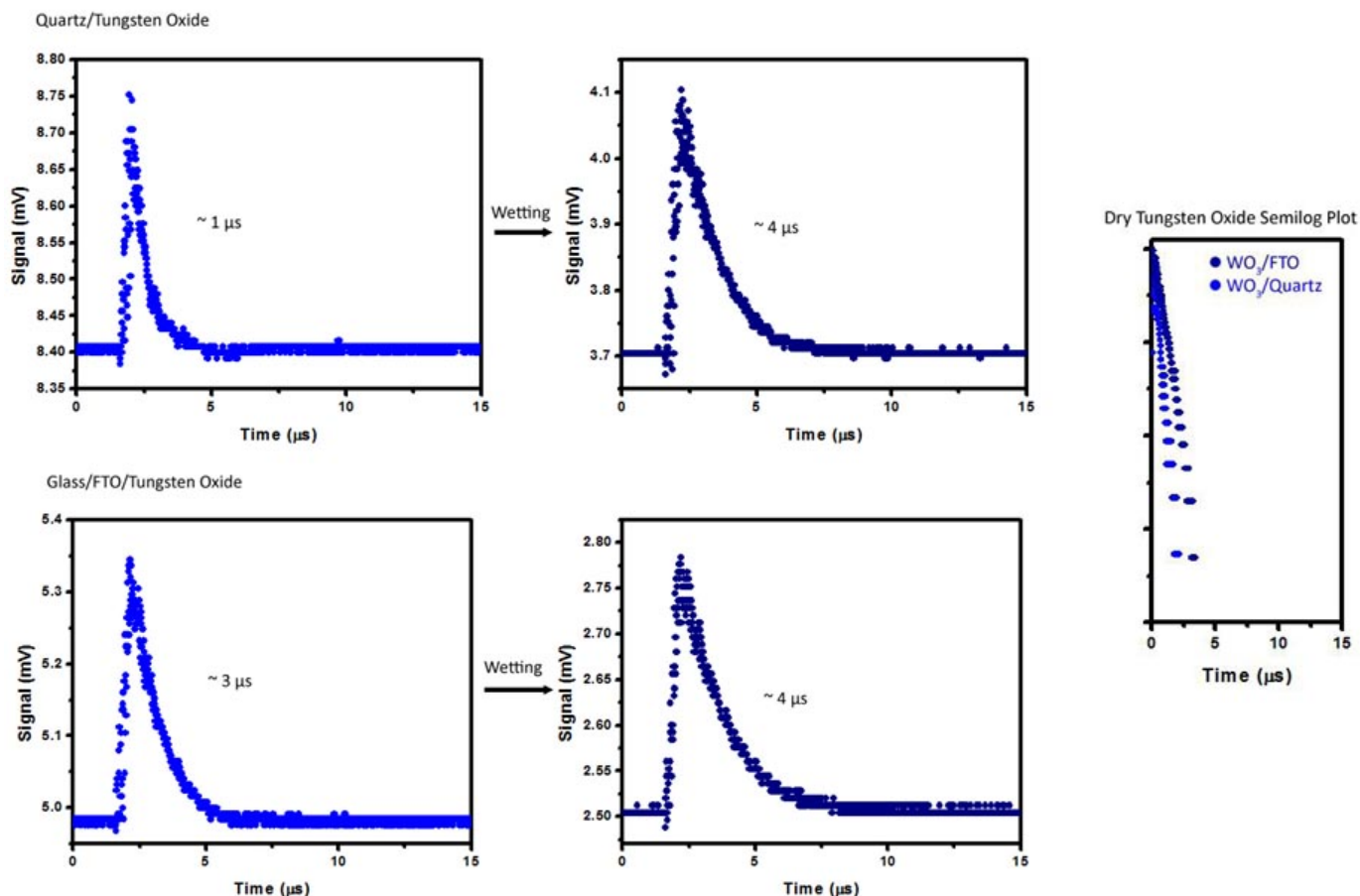


Figure 5.4 TRMC measurements with associated lifetimes for WO_3 systems. Logarithm plot included to show difference in lifetime for films grown on FTO and quartz.

From this data we can see that interfacial characteristics play an important role for thin films. Lifetime can be longer depending on the interface, which is good for solar cell applications since carrier diffusion length is proportional to the square root of carrier lifetime. This effect is diminished as the film gets thicker, however, as we will see in the next section.

5.2 Long Carrier Lifetime in Nanostructures

This study's goal was to confirm that heteronanostructures provide efficient charge separation while maintaining photocurrent and absorption as well as or better than bulk samples, which separate charges less efficiently. By comparing 25 nm thick films grown on nanonets to 25 nm thick films grown on FTO then relating that to gradually thicker films at 50, 75, and 100 nm we confirmed this hypothesis. As films got thicker, their lifetimes became more and more dominated by bulk recombination, thus were lowered. By showing that these heteronanostructures have similar recombination dynamics as thin planar films we show that this architecture gives charge separation as efficient as very thin films while greatly increasing

absorption, and therefore photocurrent. In order to provide a similar environment to a working PEC cell, all of these measurements were done under wet conditions with pH 7 water.

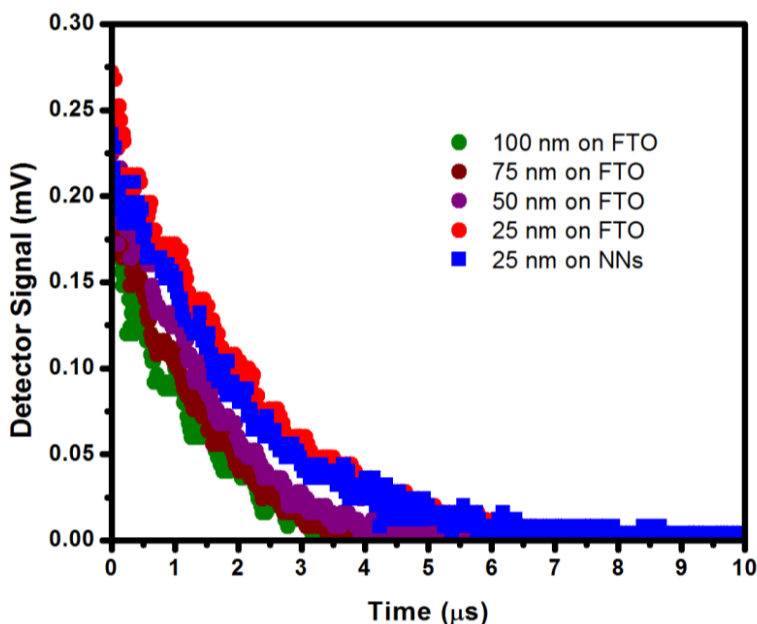


Figure 5.5 Time-domain decay plot for varied thin film thicknesses and a 25 nm film on TiSi_2 nanonets.

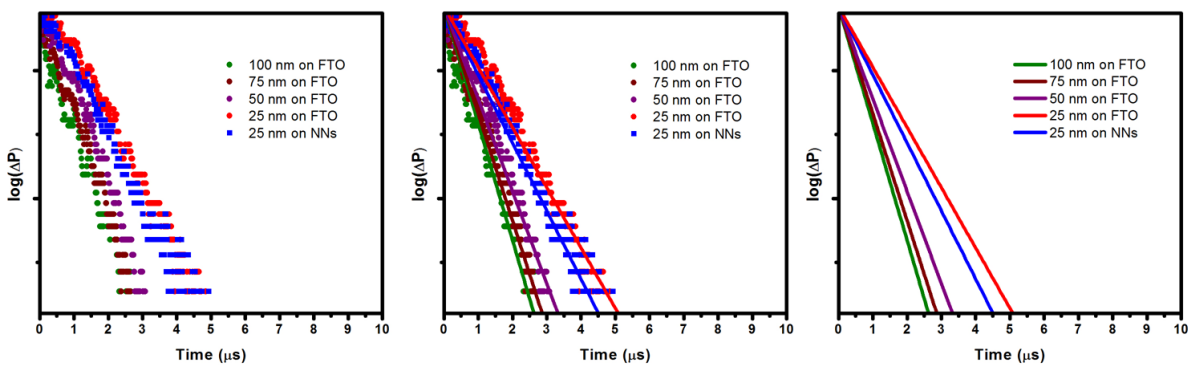


Figure 5.6 Logarithm plots with fitting according to equation 1.10. To the right the original data is omitted so that lifetime (proportional to decrease in slope) can be easily seen.

When we take into account the photocurrent for this heteronanostructure versus planar films, in which there is an over threefold increase, we can see the advantage of improved charge separation with increased light path length. Carrier lifetime for the 100 nm film is $1.1 \mu\text{s}$ while lifetime in the heteronanostructure and 25 nm film are $1.9 \mu\text{s}$ and $2.0 \mu\text{s}$ respectively. There is a small drop in lifetime between the 25 nm film on FTO and the 25 nm film on nanonets; this is likely due to competition in light absorption presented by the black nanonets or by small differences in the crystallographic orientation of Fe_2O_3 on the substrate.

5.3 Changes in Observed Lifetime with pH

When measuring carrier lifetime and recombination dynamics, the semiconductor-liquid junction played a critical role as outlined in section 5.1. This is further shown in this demonstration, tuning of the observed carrier lifetime in Fe_2O_3 and WO_3 by changing the pH of the electrolyte solution. KOH and HCl were used to adjust pH in order to minimize the effect of additional ions in solution. This effect is still in its preliminary stages of study and has not yet been reported elsewhere in literature; therefore most conclusions drawn here are speculative until thoroughly tested experimentally.

Section 1.3.1 outlines processes at the electrode surface from changes in pH. Protonation and deprotonation of surface hydroxyl groups at the interface can change the energetics of the semiconductor liquid junction. In this case, the junction becomes more receptive to holes as pH decreases, thus lifetime increases. This could be because of a change in surface chemical reactions at the electrode which could lead to an increase in lifetime. In addition, we know that changes in pH cause the chemical potential of the water oxidation reaction to change, therefore there may also be a change in the electric field at the junction; this would have an effect on band bending.

5.3.1 Iron Oxide

Iron oxide was used to test high pH solutions and show their effect on carrier lifetime. Since iron oxide dissolves in acidic solutions, tungsten oxide is used to show the effect of low pH on lifetime. As the solution became more basic, carrier lifetime decreased (figure 5.7).

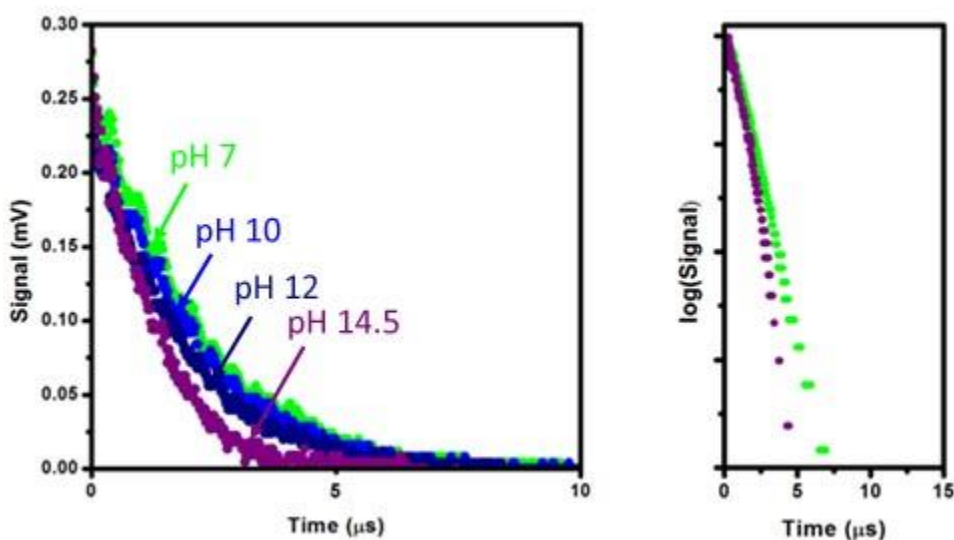


Figure 5.7 Decay and logarithm plot for 25 nm Fe_2O_3 grown on quartz and immersed in varied basic solutions. The log plot shows the difference in carrier lifetime between pH 7 and pH 14.5 solutions is significant.

From this data we can see that there is a measurable difference between lifetime in neutral conditions and highly basic conditions (pH 14.5). In basic conditions, the solution contains more OH groups and is therefore more negative. This causes the electrochemical potential of water oxidation to shift toward higher energy. In addition to this, hydroxyl groups on the surface of the photoanode which facilitate the water oxidation reaction are deprotonated at such a high pH yielding negative oxygen ions bonded to the surface of Fe_2O_3 . This excess negative charge at the interface may be what is trapping holes, though further study is needed to confirm this.

5.3.2 Tungsten Oxide

While iron oxide dissolves in acidic solutions, tungsten oxide dissolves in neutral and basic solutions yet is stable in acidic solutions. This makes tungsten oxide ideal to continue this test into lower pH values. Below are the results of measuring photoconductance decay on tungsten oxide at a variety of pHs ending at pH 7 which began to degrade the film.

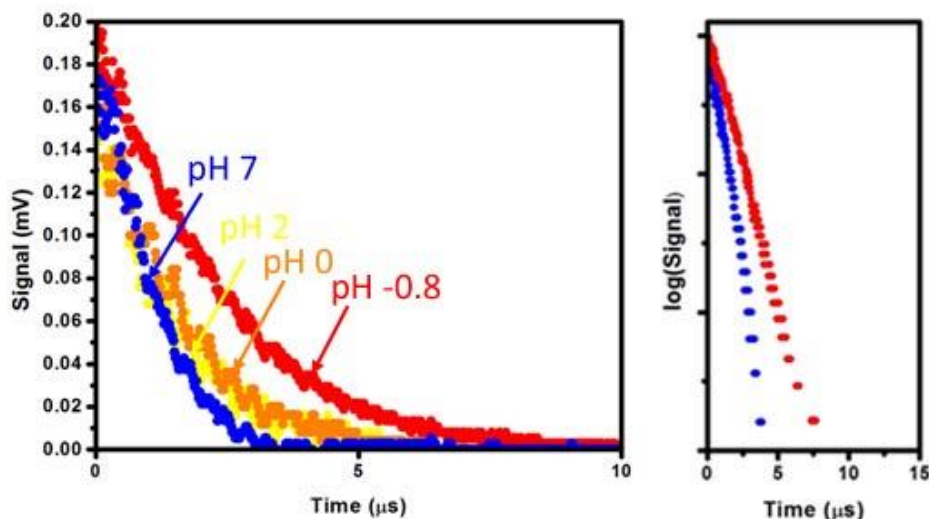


Figure 5.8 Decay and logarithm plot for 40 nm WO_3 grown on quartz and immersed in varied acidic solutions. The log plot shows the difference in carrier lifetime between pH 7 and pH -0.8 solutions and shows an even larger difference than the iron oxide system.

Thus, the same effect is seen at low pHs and it is not intrinsic only to iron oxide. Further studies are needed to understand whether or not this change in pH is caused by changes in the surface chemical reaction of water oxidation or by device physics, such as band bending. The thickness of these films being lower than the depletion width of charges at the semiconductor liquid junction may also play a role. Elements such as these can be experimentally determined using electrochemical methods, such as a Tafel plot to study overpotentials which would determine whether or not the conduction and valence bands of these materials are moving with changing pH.

Conclusions and Further Work

By introducing heteronanostructure architecture to photoanode materials, the efficiency of these materials was increased. After limited exploration using TRMC, it can be determined that these structures possess the absorbance of thick photocatalysts with charge separation along the order of thin photocatalysts. The hypothesis of this study was confirmed for both nanonets as a photoanode in a PEC cell and for tungsten oxide on silica gel as an agent to photocatalyze the degradation of 4-chlorophenol.

In order to further optimize the heteronanostructure system, a scaffold material that does not compete with light absorption such as a transparent conductive oxide should be used instead of TiSi_2 , which absorbs visible light scattered by photocatalytic thin films due to its black color. Additional electrochemical measurements also need to be integrated with carrier lifetime measurements so that these variables can be studied jointly. This will help in interpreting what processes are occurring at the semiconductor liquid junction.

In future studies, these steps can be taken to be able to paint a full picture of water splitting, the water oxidation reaction, and charge transfer in heteronanostructures. Spectroscopic measurements coupled with photoelectrochemical measurements can usually shed light on these processes. If neither, then other solid state characterization techniques and inferences from theory must be applied to this system. Solving this is just one small component of the overall goal of clean, renewable energy conversion that is being pursued by thousands of scientists around the world, and in tackling these small problems we can never lose sight of the big picture. The ultimate goal is to efficiently harvest and store energy in a usable form; both our economy and our planet depend on it.

Publications

6. Hematite-Based Solar Water Splitting: Challenges and Opportunities

Yongjing Lin, Guangbi Yuan, Stafford W. Sheehan, Sa Zhou, Dunwei Wang
Energy Environ. Sci., **2011**, Accepted

5. Semiconductor Nanostructure-Based Photoelectrochemical Water Splitting

Yongjing Lin, Guangbi Yuan, Rui Liu, Sa Zhou, Stafford W. Sheehan, Dunwei Wang
Chem. Phys. Lett., **2011**, 507, 209-215, dx.doi.org/10.1016/j.cplett.2011.03.074 (Cover Article)

4. Nanonet-Based Hematite Heteronanostructures for Efficient Solar Water Splitting

Yongjing Lin, Sa Zhou, Stafford W. Sheehan, Dunwei Wang
J. Am. Chem. Soc., **2011**, 133, 2398-2401, dx.doi.org/10.1021/ja110741z

3. Water Splitting Using Tungsten Oxide Prepared by Atomic Layer Deposition and Stabilized by Oxygen-Evolving Catalyst

Rui Liu, Yongjing Lin, Lien-Yang Chou, Stafford W. Sheehan, Wenshu He, Fan Zhang, Harvey J. M. Hou, Dunwei Wang
Angew. Chem. Int. Ed., **2011**, 50, 499-502, dx.doi.org/10.1002/anie.201004801

2. Complex Nanostructures: Synthesis and Energetic Applications

Xiaohua Liu, Yongjing Lin, Sa Zhou, Stafford W. Sheehan, Dunwei Wang
Energies, **2010**, 3, 285-300, dx.doi.org/10.3390/en3030285 (Review Article)

1. TiO₂/TiSi₂ Heterostructures for High-Efficiency Photoelectrochemical H₂O Splitting

Yongjing Lin, Sa Zhou, Xiaohua Liu, Stafford W. Sheehan, Dunwei Wang
J. Am. Chem. Soc., **2009**, 131, 2772-2773, dx.doi.org/10.1021/ja808426h

Acknowledgements

Wang group current and past members:

Prof. Dunwei Wang

Yongjing Lin

Dr. Xiaohua Liu

Dr. Huaizhou Zhao

Sa Zhou

Rui Liu

Andrew Levine

Guangbi Yuan

Matt Mayer

Zach Simpson

Jin Xie

Kenneth Aruda

Zainul Hasalani

Boston College Researchers

Dr. Dezhi Wang

Stephen Shepard

Greg McMahon

Stoichko Dimitrov

Anton Trifonov